Chemical Engineering Science 326 (2026) 123403

Contents lists available at ScienceDirect

Chemical Engineering Science

journal homepage: www.elsevier.com/locate/ces

Experimental analysis of time resolved three-dimensional velocity and vorticity fields behind single rising bubbles using Lagrangian particle tracking velocimetry

A.v. Kameke [a,*], R. Uphoff [a], E. Steuwe [a], J. H. Nissen [a], M. Hoffmann [b], M. Schlüter [b], F. Kexel [b]

[a] Faculty of Sustainable Engineering, Heinrich-Blasius-Institute, Hamburg University of Applied Sciences,
[b] Institute of Multiphase Flows, Hamburg University of Technology,

ARTICLE INFO

Keywords:
Bubble wake dynamics
3D particle tracking
Bubble induced fluid flow

ABSTRACT

The present study utilizes highly resolved Lagrange particle tracking measurements to analyze the time-dependent three-dimensional fluid dynamics in the wake of air bubbles rising in quiescent bidistilled water. Two bubble sizes are studied with regard to the velocity fields and the temporal evolution of the generated vorticity in their wakes. The range of bubble sizes is of particular interest, as it corresponds to other recent studies. The bubbles are reconstructed in three dimensions to determine the bubble rise trajectory and the bubble shape. The analysis of the aforementioned measurements, particularly the calculation of the Q-criterion, supports prior numerical findings of a wake mode exhibiting secondary vortex loops. Additionally, the energy spectra of the velocity fields and their temporal evolution are analyzed, providing a unique experimental dataset for the validation of numerical simulations and the further study of bubbly flows.

1. Introduction

The investigation of multiphase flows, particularly bubble dynamics in fluid systems, is a crucial area in fluid mechanics due to its relevance in various industrial and scientific applications such as chemical reactors and environmental studies (Schlüter et al., 2021). Understanding the behavior of freely rising bubbles is especially important, as their motion and wake dynamics influence mass transfer, mixing efficiency, and fluid structure interactions in larger multiphase systems. Single rising bubbles have been extensively studied to explore bubble-induced flow patterns and instabilities, as well as to provide fundamental insights into gas-liquid interactions (Clift et al., 1978; Magnaudet and Eames, 2000). A considerable amount of research has focused on the complex rising behavior of the bubbles using both, simulation and experiment, e.g., Cano-Lozano et al. (2016), Lee and Park (2022), Chang et al. (2023) among other important work.

Especially the complex zigzagging or helical/spiraling rising behavior of slightly non-spherical, elliptical bubbles has intrigued the community and motivated also research of the fluid flow that the bubble induces in the liquid. In Cano-Lozano et al. (2016) a phase diagram of the different bubble path styles observed in dependence on Bond (Eötvos) and Galilei numbers was obtained by precise DNS simulations. Additionally, also detailed flow field wake structures of the different bubbles are reported in this reference. In response to that work experimental research has been conducted studying the bubble rise behavior and the induced bubble wake simultaneously for single bubbles (Chang et al., 2023) and even for bubble chains (Lee and Park, 2022).

In general three main research foci dealing with single bubble rise can be found in literature: First, studies considering the complex bubble rise and its shape deformations (bubble wobbling) by analyzing the bubble trajectory and shape (Tomiyama et al., 2002; Lunde and Perkins, 1998; Kong et al., 2019) and sometimes also the surrounding fluid flow (Cano-Lozano et al., 2016; Chang et al., 2023; Lee and Park, 2022; Hoque et al., 2022). Second, studies concerned with the induced flow structures in the bubble wake regarding vorticity and drag forces (Hayashi et al., 2025) and their mutual interaction and share in (bubble induced-) turbulence (Xu et al., 2025; Ma et al., 2022; Salibindla et al., 2021). Third, studies determining the influence of bubble size, wobbling path and ambient turbulence or vortex effects on overall mass transfer (Hayashi et al., 2025; Huang and Saito, 2017b; Huang et al., 2025; Jin and Schlüter, 2019; Jin et al., 2023; Bork et al., 2005; Kameke et al., 2019a). A fundamental challenge of all studies concerned with the fluid flow around the bubbles is the precise experimental measurement of three-dimensional (3D) flow structures. Traditional measurement

* Corresponding author.
E-mail address: alexandra.vonkameke@haw-hamburg.de (A.v. Kameke).

https://doi.org/10.1016/j.ces.2026.123403
Received 21 October 2025; Received in revised form 23 December 2025; Accepted 19 January 2026
Available online 29 January 2026

techniques such as Tomographic Particle Image Velocimetry (Tomo-PIV) often face limitations in spatial resolution and accuracy, particularly in dense particle fields or when dealing with small-scale phenomena (Adrian, 1991).

One of the most significant recent advances in the measurement of fluid flows is the development of the Shake-The-Box (STB) algorithm (Schanz et al., 2016, 2021), a state-of-the-art Lagrangian Particle Tracking (LPT) method. STB combines iterative particle position refinement with temporally resolved image recording from various angles, offering highly accurate 3D trajectory reconstruction even in dense particle conditions (Schanz et al., 2016). This technique leverages temporal information and predictive particle motion models, significantly improving the robustness and precision of the tracking and velocity determination compared to conventional Particle Tracking Velocimetry (PTV) or Tomo-PIV. To the authors knowledge, only a few previous studies use this algorithm or a comparable one (Tan et al., 2019, 2020) for the measurements of the full 3D velocity fields around rising bubbles in quiescent liquid (Chang et al., 2023; Xu et al., 2025) or in induced turbulence (Xu et al., 2025; Salibindla et al., 2020, 2021).

In this work, the STB algorithm is applied to study the wake of single freely rising bubbles in great detail. In contrast to the formerly reported measurements, which use shadowgraphy and high-power LEDs to obtain particle images, here, fluorescent particles and laser illumination are used. This technique has the advantage of producing very bright particle images with a high signal-to-noise ratio and allows reducing the tracer particle size in comparison to the reported works (Chang et al., 2023; Xu et al., 2025; Salibindla et al., 2020, 2021) by a factor of ≈ 2.6 (from $d_{\text{tracer}} = 50$ μm to $d_{\text{tracer}} = 19.02$ μm). The smaller the tracer particles become, the more reliable is the assumption of passively following tracers also for the smallest scales of fluid motion which are aimed to be resolved. Especially when going to low Kolmogorov lengths of only $\eta_k = 38\mu$m as reported by Salibindla (Salibindla et al., 2020) or even lower. Here, it is estimated that the Kolmogorov length of the bubble induced fluid motion is of the order of $\eta_k = 10\mu$m when calculated from the maximal energy dissipation rate close to the bubble. The particle Stokes number of the used fluorescent tracer particles is $St = \frac{2}{9}\frac{\rho_p}{\rho_f}\frac{d_{\text{tracer}}^2}{L^2} Re \approx 3 \cdot 10^{-4}$, when calculated as in Ouellette et al. (2008) on the basis of the bubble rise velocity as a characteristic velocity and the bubble equivalent diameter as a characteristic length scale L, also for Re calculation. The fluorescent particles can be assumed to be neutrally buoyant because their density is $\rho = 1050\,\text{kg}\,\text{m}^{-3}$ and thus very close to that of water at measurement conditions ($\rho = 997\,\text{kg}\,\text{m}^{-3}$). Highly resolved 4D-PTV measurements are performed to obtain the three-dimensional unsteady velocity and vorticity wake generated by the wobbling ellipsoidal bubbles of comparatively small sizes, namely equivalent diameters $d_b = 2.45$ mm and $d_b = 2.62$ mm in bidistilled water, as have been studied experimentally with regard to mass transfer (Huang and Saito, 2017b,a; Huang et al., 2024, 2025; Kexel et al., 2021; Kameke et al., 2019b) and wake dynamics (Chang et al., 2023; Lee and Park, 2022). Also, bubbles of these sizes have been reported to have a maximal mass transfer coefficient (Huang and Saito, 2017a; Motarjemi and Jameson, 1978). Further, it has recently been reported from a numerical study that bubbles in this range exhibit a very intricate wake mode with secondary vortices (Cano-Lozano et al., 2016) and are thus especially interesting from a fluid dynamic perspective. To the best of the authors knowledge, these secondary vortices have not been confirmed by experiments yet. Albeit they are most likely of the same structures as the horse-shoe like vortices detected in the concentration wake of rising bubbles of a similar size reported by Huang and Saito and others (Huang and Saito, 2017a; Kameke et al., 2019b; Bork et al., 2005). The literature that is most often compared to in this article is summarized in Table 2. Emphasis was also laid on the correct estimation of the bubble size, since uncertainties have been reported when comparing 2D and 3D derived equivalent diameters (Chang et al., 2023). Thus a very early bubble rising state and a hypodermic needle tip is applied in this work, similar to Huang and Saito (2017a) who reported a high reproducibility of the bubble rising paths and shape deformations when different bubbles are launched under the same conditions. Due to the early bubble rising state, the bubble volume could be determined reliably when the bubble still has a spherical shape just after detachment. Mass transfer itself, however, was not part of this study since a bubble of ambient air was used in ambient air saturated bidistilled water.

The performed analysis of the bubble wake vortices and the bubble trajectory contributes to the first two research foci mentioned above, namely the investigation of the complex bubble rise and the bubble induced flow structures. To further address how the single bubble wake could influence bubble turbulence, the velocity fields in spectral space are analyzed by calculating the energy spectrum. The goal of this work is to provide some experimental data for algorithms that apply bubble forcing for bubble induced turbulence (BIT) simulations. Furthermore, to address the third focus, the obtained experimental data, the resulting particle tracks and the derived velocity fields, can in the future be used to study mass transfer rates and chemical reactions in the bubble wake for different mass transfer and diffusion coefficients. The Lagrangian particle data of the discussed experiments is made freely accessible to the community along with this publication for further studies (https://doi.org/10.15480/882.16589).

This study is organized as follows, in Section 2 the experimental setup and the measurement procedure and data analysis is detailed. In Section 3 the measurements are analyzed regarding the velocity and vorticity in the bubble wake as well as the spectral distribution of energy. The implications of the findings are discussed in detail and are related to existing results in literature. In Section 4 the main contributions of the work are summarized. Importantly, the aim is to provide detailed experimental data that can be used as a reliable reference for numeric studies.

2. Experiments

2.1. Experimental setup

The experimental setup is shown schematically in Fig. 1. The applied laser source is a high-power, dual-cavity Nd:YLF laser (Photonics Industries International, Inc., United States), with a pulse energy of 2×30 mJ at a repetition rate of 1 kHz, a maximum repetition rate of 10 kHz per cavity and emitting at a wavelength of 527 nm. The intensity of the laser depends on the operating current, ranging from 18 to 40 A, and the adjustment of the build in attenuator. In this study the laser is operated at 38 A and 90 % opened attenuator. An electronically controlled shutter controls the pulse frequency which is set equal to the image recording frequency of 800 Hz. The laser beam is directed onto volume optics via laser mirrors (Nd:YAG Mirror, Thorlabs). Volume optics consisting of module A and module C (LaVision GmbH, Germany) are used to expand the punctual laser to an illuminated volume required for the 4D-PTV measurement. Modules A and C of the volume optics each contain a cylindrical lens that expands the laser by a factor of 5 in vertical and horizontal direction, respectively. For each cylindrical lens, a corresponding focusing lens collimates the laser again. The illuminated volume is truncated by an aperture to a measurement volume with a height (y-direction) of 50 mm and a depth of 11 mm (z-direction), ensuring an homogeneous light volume across the entire width (x-direction) of the experimental vessel.

The applied reactor consists of glass panes and has a squared base of $150 \times 150\,\text{mm}^2$ and a height of 250 mm. It is filled with 2.5 L of bidistilled water containing fluorescent, monodisperse polystyrene (PS) particles with a diameter of $d_{\text{tracer}} = 19.02$ μm (microParticles GmbH, Germany). The particles have minimized dye leaching behavior and are suspended in DI-water, thus an influence on the surface tension can be neglected, which has been confirmed by tensiometric measurements using a BP50 bubble pressure tensiometer (Kruess, Germany). The water temperature is approximately constant during the measurement at 22 +/- 1 °C, at

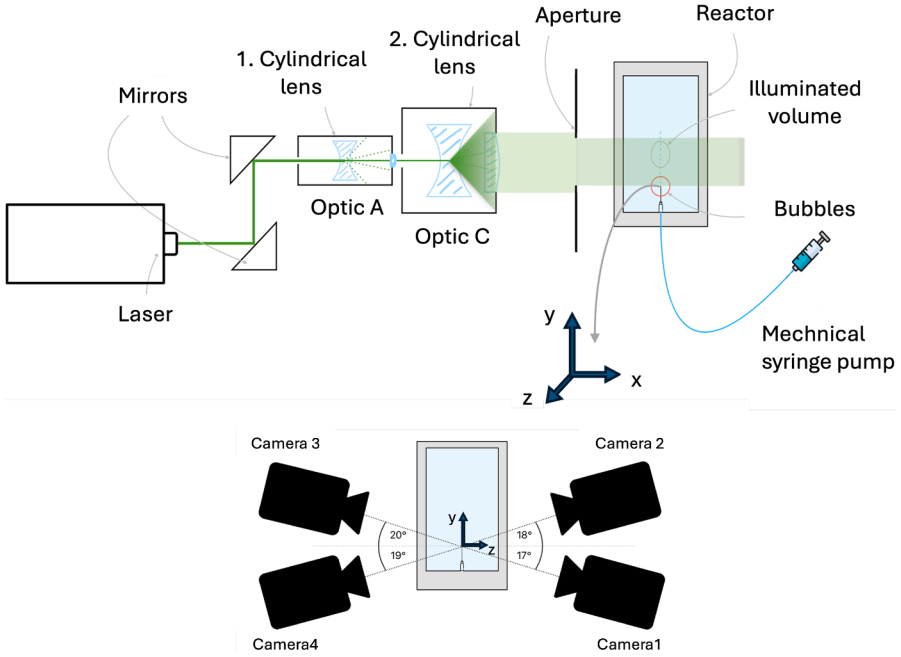

Fig. 1. Scheme of setup (top) and scheme of the camera arrangement (bottom) as viewed from the direction of the incoming laser light volume.

an ambient pressure of $p_{amb} \approx 1024$ mbar. For the generation of bubbles with highly repeatable volumes, two different Sterican hypodermic needles from B. Braun Melsungen AG (Melsungen, Germany) with outer diameters of 0.5 mm and 0.6 mm and corresponding inner diameters of 0.26 mm and 0.41 mm are used for the smaller and the larger bubble, respectively. The needles are positioned centrally in the reactor, and their facet grind ensures uniform bubble formation and detachment. The gas flow rate for bubble formation is controlled using a syringe pump (Legato 200, kdScientific, Massachusetts, USA). The bubbles are generated at a frequency of 0.58 Hz for the smaller needle diameter and 0.50 Hz for the larger one.

The measurement volume in this study has a size of $L_x \times L_y \times L_z \approx 35 \times 47 \times 11\,\text{mm}^3$, where L_x corresponds to the width of the overlap of the field of view of the image sections captured by the four cameras, L_z is defined by the extent of the laser light volume and L_y results of the overlap of field of view of all four cameras and the illuminated volume. L_y is therefore smaller than the laser light volume height due to the restricted fields of view from the cameras. Two different measurement volumes are studied, an upper volume and a lower volume, both of the commented size. The lower volume is located directly above the needle tip, so that the bubble wake could be investigated directly starting from the detachment of the bubble from the needle. For the evaluation of the data the needle tip is set to the world coordinate origin. All space coordinates shown in the figures are in reference to this coordinate origin.

Four Phantom VEO 640L (Vision Research Inc., United States) high-speed cameras with $1600 \times 2560\,\text{pixel}^2$ are arranged in orthogonal planes with respect to the direction of the incoming laser light. The cameras record the illuminated volume at oblique angles rather than perpendicularly, as shown in Fig. 1. Two of the cameras are located on each side of the reactor so that the camera pairs are aligned in opposite directions. Their positioning differs slightly in angle, up to a maximum of 20° to the plane perpendicular to $\vec{g}$. Each camera is equipped with a Milvus 1.4/50 from Carl Zeiss AG (Oberkochen, Germany) with a focal length of 50 mm and an aperture range of f/1.4 to f/16. In addition, a magnification ring with a thickness of 20 mm is mounted in between each camera and its lens in order to achieve a suitable resolution down to 20.3 µm/pixel which roughly corresponds to the diameters of the tracer particles, even though these appear on average as white blobs on approximately 3×3 to $5 \times 5\,\text{pixel}^2$. To adjust the focal plane inclination, Scheimpflug-adapters are used on each camera. To prevent laser light to directly enter the cameras, e.g. by reflection on the bubble surface, four high-pass filters (90 % transmission for $\lambda_e > 540$ nm) are installed directly on the lenses.

2.2. Calibration

A 3D calibration is performed to map the real world object space (x, y, z) to the images on the four camera chips $(x_i', y_i'), i \in (1, 2, 3, 4)$. A calibration target (model 058-5, LaVision GmbH, Germany) with dimensions of $58 \times 58\,\text{mm}^2$ is aligned with the laser volume and positioned at the center of the light volume for the adjustment of the focal plane of each camera. The target is then moved to four additional positions, two towards camera 1 and two away from it with a distance of 4.25 mm between each pair of calibration planes while taking images at all five target position with all cameras. The camera images are then calibrated using the DaVis 11.0 software (LaVision GmbH, Germany). Optical distortion and perspective effects are modeled using a third-order polynomial, and interpolation is applied between recorded target planes.

In the next step, volume self-calibration (VSC) is performed to optimize the previously performed calibration based on the particle images (Wieneke, 2008, 2018). The VSC is performed using the brightest particles first and the perspective calibration is corrected using the disparity vectors. This process is an iterative procedure that is terminated by the user when both, the mean and the maximum disparity, are less than 0.1 voxel corresponding to approximately 2 µm. The final mean resolution is 49.3 pixel/mm or 20.3 µm/pixel, with a maximum fit error of 0.063 pixels, corresponding to 1.3 µm. Finally, the optical transfer function (OTF) of the particle images is calculated. This allows, after the perspective correction of the VSC, to significantly reduce the effects of potential distortions caused by a shallow depth of field or distortion by the optics used on the reconstruction of virtual camera particle images, thus enabling a more accurate evaluation of the particle positions especially in depth (z-direction) (Schanz et al., 2013).

2.3. Measurement procedure

The 4D-PTV measurements are performed with the objective of conducting a precise analysis of the trajectories of the tracer particles in

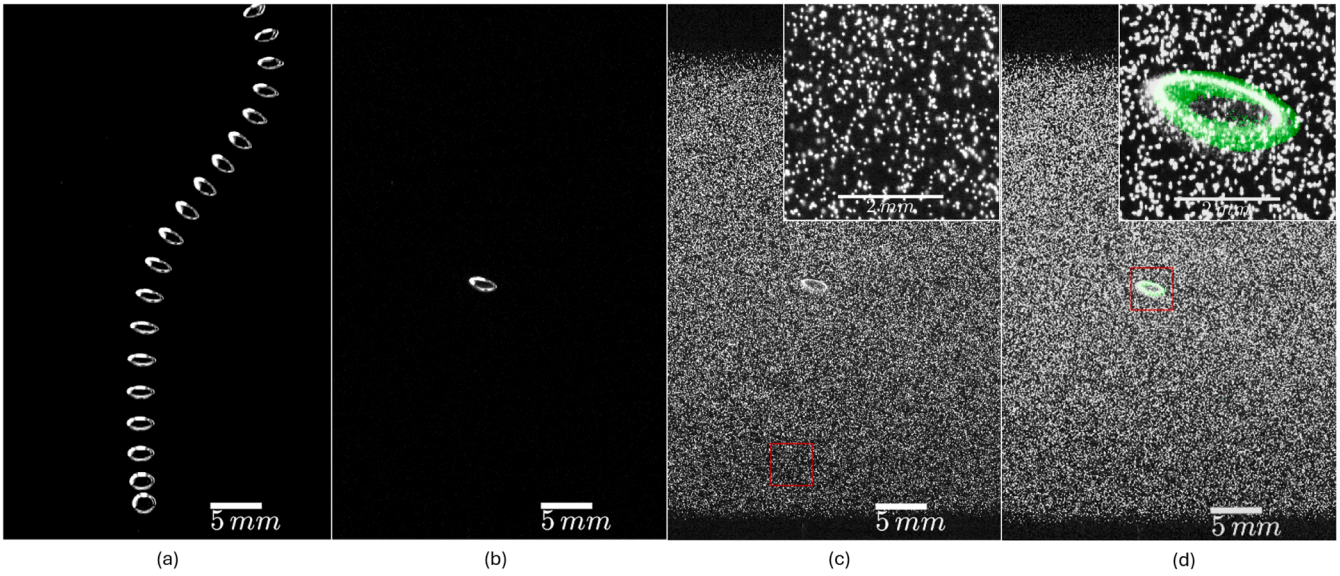

Fig. 2. Representation of the generated images of bubbles in bidistilled water with suspended fluorescent tracers. (a) Accumulated image of the bubble at different times ($\Delta t = 0.01$s) with white LED illumination. (b) Single image of a bubble rising illuminated with the white LED. (c) A different bubble and fluorescent particles illuminated with laser light. (d) Overlaying images (b) in transparent green and (c) in black and white. This shows that different bubbles always rise along the same path.

the bubble wake. The measurements are carried out and analyzed using the DaVis 11.0 software with the STB module, following the steps outlined below in more detail. MATLAB (Matlab, 2024) is used for further image processing, graphical representation, and evaluation of the data. With a slight modification of the experimental set up, it is also possible to record a bubble without the particles. Instead of the laser light, two white LED panels serve as illumination from above and from the side (same direction as the laser) in order to be able to record the bubble contour on all four cameras. Fig. 2 shows the pre-processed images of a bubble and the suspended particles. When using the LED illumination only the bubble becomes visible, as in Fig. 2 (a) and (b), while the laser illuminates the particles and the bubble, as in (c).

In the subfigure (a) an accumulated image of the same bubble rising through the measurement volume as recorded by camera 1 is shown. The accumulated image is generated by superimposing every eighth frame, corresponding to a temporal spacing of $\Delta t = 0.01$ s between consecutive images. In image (b) a single processed snapshot of the bubble rise is shown. For noise reduction and outline detection the background is subtracted using MATLAB. Images like these are later on used for the bubble shape and path reconstruction from all four cameras. In (c) an image of particles and a bubble is shown. The background is subtracted and the intensities of the particles are normalized and intensified using DaVis. In image (d), the two different bubble images (b) and (c) are superimposed (bubble from (b) in transparent green). This shows that the bubbles look almost identical and rise along the same trajectory in the reactor during each experimental run. It should be noted that images (b) and (c) show two different bubbles on the same rising height, generated under identical conditions and recorded at the same frame rate of 800 Hz.

The further evaluation of the measurements is divided into two subsections, the reconstruction of the bubble trajectory and its shape (2.4) and the representation and reconstruction of the Lagrangian paths of the tracer particles using STB from which the velocity and vorticity fields are derived (2.5). The results of both analyses are then overlaid. Thereby, the velocity, the vorticity and other quantities from the liquid phase can be linked to the bubble behavior and the course of the bubble trajectory.

2.4. Reconstruction of bubble trajectory and bubble shape

The reconstruction of the rising bubbles enables a detailed analysis of their shape, size, and motion. Each camera view of the LED-illuminated bubble is processed individually in MATLAB. At each time step images are smoothed and thresholded to generate binary masks, from which bubble contours and centroids are extracted. The resulting centroid position trajectories for each camera are smoothed applying a smoothing spline and reconstructed into a 3D bubble trajectory via triangulation, using a custom MATLAB code and the DaVis calibration function. Bubble shape reconstruction is performed in two complementary ways, from a 3D reconstruction of the bubble and from the average of the 2D camera images. For the 3D bubble shape reconstruction the 2D contours are projected into 3D object space along their respective lines of sight using the DaVis calibration. Tube-like volumes are generated for each camera view using MATLAB's *alphaShape* function, and their intersection defines the bubble volume. A $100 \times 100 \times 100$ bounding grid is used to identify interior points, whose convex hull yields a closed 3D surface mesh for further analysis and visualization.

While the described method enables the volumetric reconstruction of the bubble, its accuracy is limited by the almost collinear camera positions imposed by the reactor geometry. This results in reduced resolution in the z-direction, particularly affecting surface details causing the bubble to have a rhombus shape when viewed from the z-direction. Nevertheless, the reconstruction reliably captures the bubble's overall dynamics. The equivalent bubble diameter is then calculated from the 3D mesh. To do so, the reconstruction is projected onto the (x, y)-plane, and an ellipse is fitted to the projection. The bubble is approximated as an oblate ellipsoid with principle semi-axes a, b, c, with $c = a > b$. This provides a practical means to compute the volume equivalent diameter ($d_\mathrm{b} = 2\sqrt[3]{a^2 b}$) along the bubble rising trajectory. However, as can be observed in Fig. 2 (a) the bubble shape deviates from an ellipse due to surface shape oscillation and out of plane rotation, yielding an error in the equivalent volume. Therefore, the following analysis utilizes the equivalent diameter of the bubble at the moment of detachment from the needle tip when it still is of nearly spherical shape.

Alternatively, the bubble shape is estimated directly from the 2D image data by fitting an ellipse to each camera view individually and

calculating the volume from the resulting major and minor axes, again under the assumption of rotational symmetry. The equivalent bubble diameter is then obtained by averaging the four diameters calculated from each camera perspective with the mean resolution for each camera. While this method is computationally simpler, it does not account for projection distortions and resolution correction for the movement of the bubble in y-direction that are necessary because of the tilted angle of the cameras with regard to the calibration target. However, the bubble wobbling frequency is more clearly pronounced using this 2D-based procedure and therefore it is used for the calculation of the bubble semi-axes shown in Figs. 3 (d), (f) and 4 (d), (f). The two values of the bubble equivalent diameter right after bubble detachment from the 2D and 3D based reconstructions are $d_{b2D} = 2.58\,\text{mm}$ and $d_{b3D} = 2.32\,\text{mm}$ for the smaller bubble and $d_{b2D} = 2.60\,\text{mm}$ and $d_{b3D} = 2.64\,\text{mm}$ for the larger one. These values are averaged for each bubble size to yield the values as stated in Table 2. The standard error of this two measurements gives the stated measurement uncertainty. The uncertainty in equivalent diameter from these two different reconstruction methods is considerably larger than the mean standard deviation of different bubbles of the same size along height which, for both methods, is below $0.022\,\text{mm}$, since all bubbles rise nearly identical. The resulting equivalent diameters serve as the basis for evaluating dimensionless numbers such as the Eötvös (Eo), Reynolds (Re), Morton (Mo), and Galilei (Ga) numbers, defined below.

2.5. Particle tracking using Shake-the-Box (STB)

Tracer particle trajectories are analyzed using the advanced variable Time-Step Shake-The-Box (VT-STB) method. This approach extends the STB method developed by Schanz et al. (2021), Schröder and Schanz (2023) and improves tracking accuracy in highly dynamic flows with a wide range of particle velocities, such as a bubble rising in a quiescent liquid. In conventional STB methods, the coexistence of slow- and fast- moving particles causes tracking ambiguities and ghost particles. VT-STB addresses this issue through an iterative tracking procedure with variable time steps, enabling more reliable particle trajectory reconstruction.

Particle trajectories are recorded at a frame rate of 800 Hz within a processed volume of $1685 \times 2159 \times 470$ voxels. For each bubble rise, approximately 1000 time steps after bubble detachment are stored. The VT-STB method first applies larger time steps to track slow-moving particles located far from the bubble. The time step is then progressively reduced to capture faster particles in the bubble wake, while intensities of previously reconstructed particles are removed from the camera images. This iterative approach improves tracking accuracy by reducing incorrect particle assignments and reliably identifying both slow- and fast-moving particles.

The accuracy of reconstructed 3D particle positions in Lagrangian particle tracking methods such as STB is closely related to the quality of camera calibration and the consistency of particle image projections across all views (Wieneke, 2008). Several sources of error are evaluated and considered during processing. First, the calibration error is estimated from the calibration procedure using a 3D calibration as mentioned above. This calibration error is then further reduced by applying Volume Self-Calibration, where the lines of sight from all camera images of a single particle are drawn using the calibration information. If there were no calibration errors, these lines would intersect at a single point in object space (world coordinates). However, due to effects such as vibrations and misalignment, a so-called triangulation error in object space remains, and the various lines of sight enclose a small volume. The true particle position in object space can then be estimated as the center of this volume. If this new particle position is backprojected to the camera images using the calibrated mapping functions, a disparity vector to the original intensity peak in each camera image can be drawn. The backprojection error quantifies the mean squared difference between the backprojected 3D particle position and the acquired 2D image position for each camera. By minimizing this backprojection error through adjustments of the mapping functions, the calibration can be further improved, reducing the maximal triangulation error to below 0.1 voxels (Wieneke, 2008, 2018; LaVision GmbH, 2023). The position uncertainty for each particle at each time step can also be derived from the so-called "Shake" step in the Shake-the-box algorithm. Here, the extrapolated particle position in world coordinates is perturbed slightly ("shaked") to minimize the residual intensity peaks in each camera image. The remaining uncertainty is then quantified by a residual value (Schanz et al., 2016). According to the methodology described by Schanz et al. (2016) and based on the optical configuration used in this study with approximately 0.017 particles per pixel, the typical positional error resulting from the Shake-the-Box algorithm should be below 0.002 pixels which corresponds to $0.041\,\mu\text{m}$ and is thus of the order of the maximal fit error from the calibration and the maximal error reported in the Volume Self-Calibration. The resulting value reflects the local fit quality and serves as a lower bound for the true positional error under ideal conditions (Schanz et al., 2016; Gesemann, 2015). In practice, however, additional error sources might add to the overall uncertainty such as image noise, particle overlap, and tracking ambiguities (Gesemann, 2015; Sciacchitano et al., 2013). Consequently, actual 3D particle position uncertainties are often one or two orders of magnitude higher, ranging from 5 to 20 μm depending on the optical setup and flow conditions (Bhattacharya and Vlachos, 2020).

Table 1
Average particle position uncertainties of the data sets in all three dimensions.

Data	Av. uncertainty x	Av.uncertainty y	Av. uncertainty z
$d_b = 2.45\,\text{mm}$ low FOV	0.38 µm	0.57 µm	2.3 µm
$d_b = 2.45\,\text{mm}$ high FOV	0.29 µm	0.50 µm	2.1 µm
$d_b = 2.62\,\text{mm}$ low FOV	0.24 µm	0.38 µm	1.5 µm
$d_b = 2.62\,\text{mm}$ high FOV	0.35 µm	0.60 µm	2.5 µm

The DaVis software estimates a position uncertainty for each particle position at each timestep. The position uncertainties given by DaVis in this study are lower than these estimates from literature (Bhattacharya and Vlachos, 2020) but are approximately one order of magnitude higher than the error estimated with synthetic data from STB (Schanz et al., 2016). To derive a positional uncertainty the DaVis software applies a polynomial least-squares fit along each particle trajectory, with the uncertainty corresponding to the confidence intervals of the fitted coefficients (Schröder and Schanz, 2023; Janke and Michaelis, 2021). The average uncertainties of all tracks in each of the three spatial dimensions are reported in Table 1.

2.6. Processing of tracks and derivation of velocity field

The needle tip is set as the reference point $(x, y, z) = (0, 0, 0)$ in the 3D object space by adding an offset to the trajectory data of the tracer particles. A gaussian filter of a kernel size of 6 time steps is applied in MATLAB to further smooth the trajetory measurement data (built-in function *smoothdata*). Tracks that are shorter than 9 time steps are disregarded.

To reduce remaining interruptions in the particle tracks, a track extrapolation and reconnection algorithm is developed in MATLAB. Existing tracks are extrapolated forward and backward in time over $t_n = 5$ time steps using first-order polynomial fits based on the $n = 13$ start or end points of each track. The extrapolation is performed independently for each spatial dimension. Extrapolated positions are compared to identify plausible connections between track ends and beginnings. A matching score, defined as the sum of squared differences between extrapolated positions across all spatial dimensions, is evaluated against a dynamic threshold. This threshold is based on the 99^{th} percentile of past prediction errors and scaled by a factor of five to account for uncertainty and noise. Only connections below this threshold are accepted. Track pairs are iteratively evaluated, selecting the pair with the

minimum matching error. Once connected, missing segments are filled using third-order polynomial interpolation, and the original fragmented tracks are removed.

The reconnection quality is assessed by visual inspection, revealing successful reconnections particularly in regions shadowed by the bubble in the laser light volume. The procedure increases track continuity and raises the number of tracks spanning the full measurement duration (≈ 1 s) by about 10 %. Particle velocities along the reconstructed trajectories are computed using a fourth-order central difference scheme. To enable the resolution of velocity gradients in the bubble wake and the derivation of quantities such as vorticity and the Q-criterion at spatial resolutions of a few hundred microns, remaining erroneous tracks with implausible velocities are filtered out. For this purpose, particle positions at each time step are used to generate a tetrahedral mesh via MATLAB's Delaunay triangulation. Tracks with velocities deviating by more than 5σ from the mean velocity of neighboring particles are discarded.

Finally, particle velocities are smoothed independently in each spatial direction using the MATLAB smoothing spline routine *csaps* with a smoothing factor of $s_{\mathrm{vel}} = 0.9999925$. After processing, approximately 65,000-70,000 trajectories are obtained per time step, of which 20,000-22,000 span the entire duration of recording. These trajectories are then used to reconstruct the Eulerian velocity field and its gradients, yielding a 3D velocity field $\vec{v}(x, y, z, t_i)$ for each time step, from which vorticity and the Q-criterion are derived.

In particular, the scattered velocity data from all tracer particle trajectories is interpolated for each time step using again Delaunay triangulation to connect the scattered track coordinates to derive a 3-D function F_i for each velocity field component $\vec{v} = (u, v, w)^T$ that satisfies $u = F_u(x, y, z)$ on the scattered particle positions (x, y, z). The same is done for the remaining velocity components v and w (built-in MATLAB function *scatteredInterpolant*). The functions F_i are then evaluated at discrete cartesian grid points using a linear interpolation scheme. Here, the resolution of the grid can be deliberately chosen, but the real resolution depends on the density of the reconstructed trajectories. For the gained data the average volume per particle is around $0.24\,\mathrm{mm}^3$ and thus the average resolution in each direction $res_{real} = (0.24\,\mathrm{mm}^3)^{1/3} \approx 0.62\,\mathrm{mm}$. For the resulting Eulerian velocity field a slight oversampling is however beneficial and the grid resolution is chosen to be a third of res_{real}, namely $res_{Euler} = 0.2\,\mathrm{mm}$. In this way, even the flow behind the smaller bubble is well resolved with 15 different velocity values along the major axis a of the bubble where $2a \approx 3\,\mathrm{mm}$.

3. Experimental results and discussion

3.1. Bubble rise velocity, trajectory and shape

Figs. 3 and 4 illustrate the representative rise of bubbles with equivalent diameters of $d_{\mathrm{b}} = 2.45\,\mathrm{mm}$ and $d_{\mathrm{b}} = 2.62\,\mathrm{mm}$ respectively, directly from their detachment points at the needle-tip onward. The bubble's center, as projected from all camera perspectives, was used to trace its world coordinate trajectory as described in Section 2.4. Immediately after detachment, it is evident that the bubble has an almost spherical contour in both cases, and all principal axes are of equal size. However, as it rises, its shape shifts from a spherical contour to an ellipsoidal one. Furthermore, throughout the entire ascent, the bubble's shape continuously changes, exhibiting characteristic wobbling motion, causing periodic changes of the ellipsoidal principal semiaxes (so called mode 2.0 oscillations) and its rise velocity (see Figs. 3 and 4 (a), (d) and (f)). The frequency of this wobbling is around $f_w = (68 \pm 3)\,\mathrm{Hz}$ for the larger bubble and $f_w = (89 \pm 1)\,\mathrm{Hz}$ for the smaller bubble which fits the observations by Lunde and Perkins (1998) for ellipsoidal bubbles of similar sizes rising in quiescent water. In this work, the wobbling frequency is determined in two ways: Firstly by analyzing the frequency of the semiaxes aspect ratio wobbling using a Fourier transform as shown in Fig. 3 (f) and secondly by evaluating the frequency by hand, counting the number of oscillation maxima and dividing by the time difference. From this comparison the uncertainty of the measurement was estimated. Lunde and Perkins compare their experimental results to numerical work (Meiron, 1989) and develop a simple model for the shape oscillations of spheroids expanding the analytical expression of Lamb (2009) for spherical bubbles. The derived formula

$$f_{w_{\mathrm{theo}}} = 1/(2\pi)\sqrt{16\sqrt{(2)}\cdot\xi^2)/(\xi^2+1)^{1.5}}\sqrt{\sigma_l/(\rho_l\cdot(d_{\mathrm{b}}/2)^3)} \tag{1}$$

that is also used in Kong et al. (2019) results in $f_{w_{\mathrm{theo}}} = (78.74 \pm 0.80)\,\mathrm{Hz}$ and $f_{w_{\mathrm{theo}}} = (89.40 \pm 0.13)\,\mathrm{Hz}$ for the values of ellipticity along rising height for the larger and the smaller bubble investigated. Here, $\xi = \frac{d_{\mathrm{b}}^3}{8(d_{\mathrm{b}}/2)^3}$ is the ellipticity and σ_{l} and ρ_{l} are the surface tension and the density of clean water at experiment temperature. As also noted in Kong et al. (2019) the bubble undergoes additional oscillations due to detachment from the needle tip in the beginning of the bubble rise. These are pronounced during the acceleration phase of the bubble for the first $\approx 15\,\mathrm{mm}$ of the rising trajectory and are thus not used for the determination of the wobbling frequency. While the prediction of the bubble wobbling frequency of the smaller bubble is in very good agreement with theory, the frequency of the larger bubble is lower than expected. An experimental value that is lower than the predicted one was also observed by Lunde and Perkins (1998) themselves for larger bubbles.

Focusing on the bubble's rising path, the bubble center initially follows a nearly vertical ascent over the first $\approx 15\,\mathrm{mm}$ for the larger bubble and the first $\approx 20\,\mathrm{mm}$ for the smaller one. The behavior of both bubbles is comparable to the linear ascent section (LAS) observed by Huang and Saito for clean water experiments (Huang and Saito, 2017b,a) and the values obtained in recent experiments with a similar bubble size (Lee and Park, 2022). Acceleration occurs over this interval, as shown in the bubble's (x, y)-positions in Figs. 3 (b) and 4 (b) and their velocity profiles Figs. 3 (c) and 4 (c). Beyond this point, the ellipsoidal bubble begins to deviate from its linear rising path. The first inversion section ends with the inflection point, where the $x(y)$-function has its steepest slope (indicated by the red dot in Fig. 3(b) and 4(b)). The bubble's rise is not only characterized by a zigzag motion in the (x, y)-plane but also by a slight translation in the z-direction (Figs. 3 (e) and 4 (e)). This movement indicates the beginning of a flattened spiral motion as expected from the phase diagram from numerical work (Cano-Lozano et al., 2016). Thus, with the applied setup, comparable bubble trajectories to those in the experiments of Huang and Saito (Huang and Saito, 2017b) are achieved, especially for the larger bubble which is to expect, as the inner diameters of the hypodermic needles are very similar (0.40 mm in Huang and Saito (2017b,a) and 0.41 mm in the present study). Although the bubbles investigated by Huang and Saito (2017b,a) have a slightly higher equivalent diameter of $d_{\mathrm{b}} = 2.9\,\mathrm{mm}$ than the larger bubble $d_{\mathrm{b}} = 2.62\,\mathrm{mm}$ analyzed in this study, the end of the linear ascending section was located at approximately the same position. The first inversion section, the first inflection point and the second inversion section for the uncontaminated water case are slightly lower in Huang and Saito (2017b,a) when compared to the smaller bubble with $d_{\mathrm{b}} = 2.45\,\mathrm{mm}$ in this study, but highly similar to those of this study's larger bubble with $d_{\mathrm{b}} = 2.62\,\mathrm{mm}$. It is also observed that the rising behavior of five independently ascending bubbles is nearly identical, as also previously reported (Huang and Saito, 2017a). To provide evidence for the repeatability of the bubble rise trajectory, the first inflection points of five different rising bubbles of $d_{\mathrm{b}} = 2.45\,\mathrm{mm}$ are analyzed. The standard deviations of the inflection point positions are found to be $(\sigma_x, \sigma_y, \sigma_z) = (0.045, 0.090, 0.17)\mathrm{mm}$, which is only 2–7 % of the equivalent diameter of the smaller bubble size. The percentage variations are similar for the larger bubble. The comparability of the contours and the associated semiaxes of different bubbles has been discussed in Section 2.4. The good comparability is also visually emphasized by Fig. 2 (d), that shows that the bubble contours of two randomly selected bubbles of the same size at the same rising height exhibit an almost identical shape.

The equivalent diameter d_{b} measured as described in 2.4 is used for the evaluation of the dimensionless numbers such as the Eötvös number

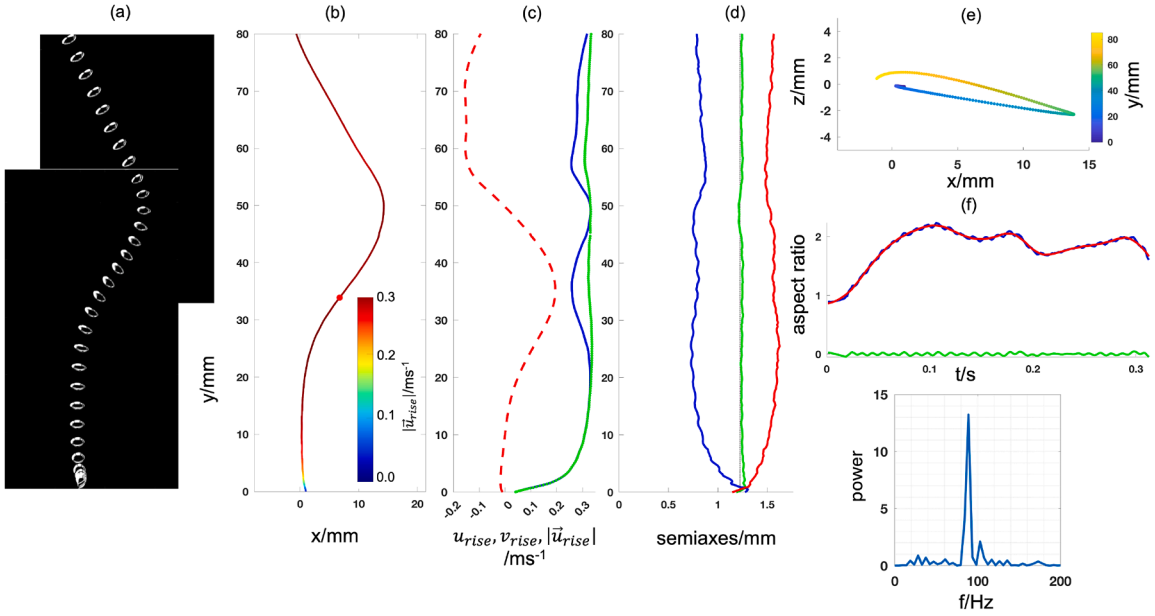

Fig. 3. (a) Accumulated image of the bubble rise at different times for the smaller bubble of $d_b = 2.45$ mm as viewed from camera 1 for both measurement heights. (b) The bubble centroid trajectory reconstructed in the object space from all four camera views and projected to the (x, y)-plane for plotting with first inflection point as red dot. (c) Absolute- (green dotted), vertical- (blue line) and x-direction- (red dashed) bubble velocity, all slightly smoothed, to suppress the influence of the wobbling. (d) The mean principal semiaxes (blue and red) are obtained here as a mean value from ellipsoidal fits to all four camera perspectives from which the equivalent radius is obtained (green). The equivalent radius for $r_b = 1.225$ mm is indicated by a faint vertical black line. Oscillations can be clearly observed along the full bubble rise. (e) Shows the movement of the bubble center in the z-direction (depth) and confirms the beginning spiralling motion. (f) The aspect ratio of the semiaxes ξ shows the same periodic changes as the semiaxes. The raw data (red dotted line) is compared to smoothed data (blue cont. line) and the difference of both (green line) is shown as oscillations around zero. The frequency of these oscillations is analyzed to be $f_w = (89 \pm 1)$ Hz using a Fourier transform, see text.

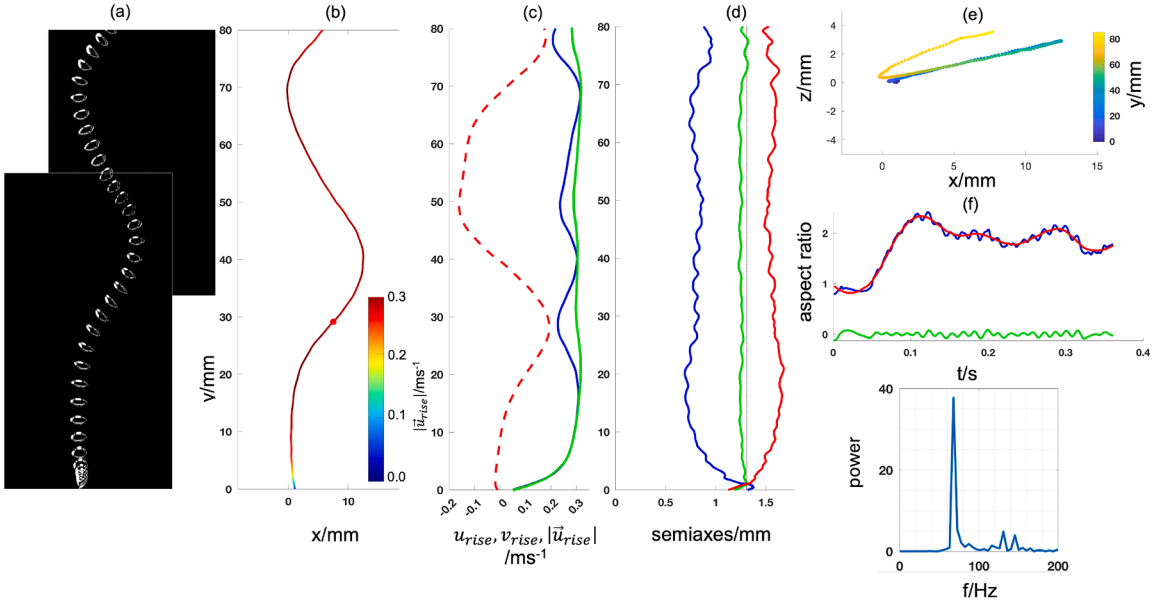

Fig. 4. (a) Accumulated image of the bubble rise at different times for the larger bubble of $d_b = 2.62$ mm as viewed from camera 1. (b) The bubble centroid trajectory reconstructed in the object space from all four camera views and projected to the (x, y)-plane for plotting with first inflection point as red dot. (c) Absolute- (green dotted), vertical- (blue line) and x-direction- (red dashed) bubble velocity, all slightly smoothed, to suppress the influence of the wobbling. (d) The mean principal semiaxes (blue and red) are obtained here as a mean value from ellipsoidal fits to all four camera perspectives from which the equivalent radius is obtained (green). The equivalent radius for $r_b = 1.31$ mm is indicated by a faint vertical black line. Oscillations can be clearly observed along the full bubble rise. (e) Shows the movement of the bubble center in the z-direction (depth) and confirms the beginning spiralling motion. (f) The aspect ratio of the semiaxes ξ shows the same periodic changes as the semiaxes. The raw data (red dotted line) is compared to smoothed data (blue cont. line) and the difference of both (green line) is shown as oscillations around zero. The frequency of these oscillations is analyzed to be $f_w = (68 \pm 3)$ Hz using a Fourier transform, see text.

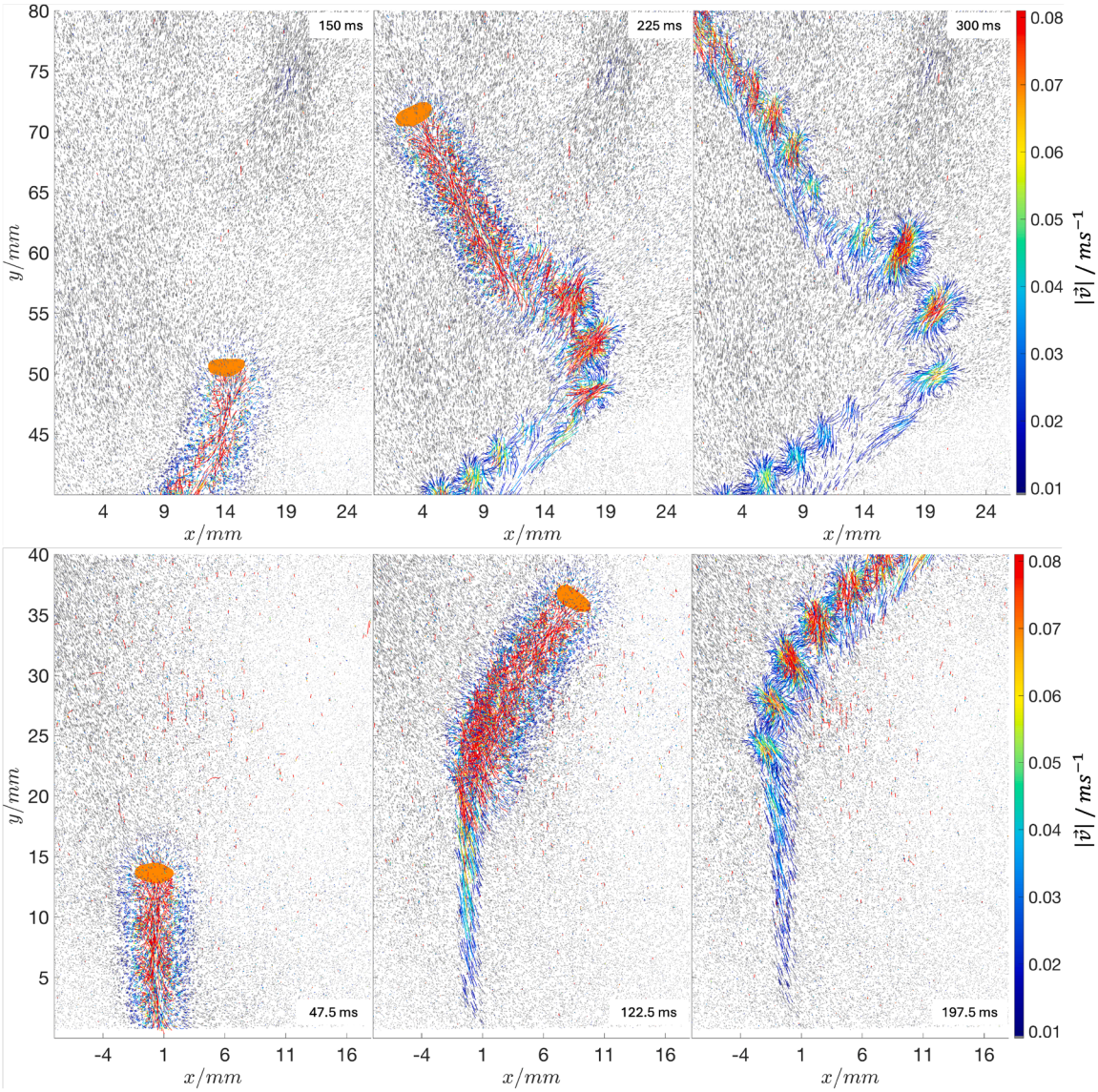

Fig. 5. Tracer particle trajectories with the velocity magnitude shown in a color gradient for a bubble equivalent diameter of $d_b = 2.45$ mm. The particle trajectories shown here are those that are retrieved from the DAVIS software without any further postprocessing. The slow, barely moving particles are shown in light gray to improve the visualization of the moving ones. Some outliers of particle trajectories that are erroneously detected in the DAVIS software and have a high velocity (red) albeit the neighboring particles are almost still (gray) can also be observed. These outliers are subsequently filtered out using a custom made MATLAB script (not shown). The figure is to be read from the lower left to the upper right. The timestamps indicate the elapsed time after bubble detachment in the corner of each image. Note that the data in the lower panel and the upper panel are not from the same measurement but from measurements under the same conditions but with different field of views as detailed above.

(Eo), Reynolds number (Re), Morton number (Mo) and Galilei number (Ga). The Eötvös

$$Eo = \frac{\Delta\rho \cdot g \cdot d_b^2}{\sigma}, \tag{2}$$

number quantifies the balance between buoyancy and surface tension forces, where $\Delta\rho$ is the density difference, g the gravitational acceleration, d_b the equivalent bubble diameter, and σ the surface tension.

The Reynolds number

$$Re = \frac{|\vec{u}_{rise}| \cdot d_b \cdot \rho}{\mu} \tag{3}$$

characterizes the ratio of inertial to viscous forces, with $|\vec{u}_{rise}|$ as the terminal bubble rise velocity, ρ the fluid density, and μ the dynamic viscosity.

The Morton number

$$Mo = \frac{g \cdot \mu^4 \cdot \Delta\rho}{\rho^2 \cdot \sigma^3} \tag{4}$$

relates fluid properties to interfacial behavior. While the Galilei number

$$Ga = \frac{g\, d_b^3\, \rho^2}{\mu^2} \tag{5}$$

expresses the ratio of the influence of gravitational and viscous forces.

To facilitate comparison between the present measurements and values reported in the literature, Table 2 summarizes the relevant dimensionless numbers for each study compared to in this paper, together with the terminal rise velocities $|\vec{u}_{rise}|$ and bubble equivalent diameters d_b, where available. In addition, comparison with the work of Clift et al. (1978) shows that the terminal rise velocities measured in this study agree well with those reported for bubbles in uncontaminated, clean systems (cf. Supplementary Information), which also indicates the

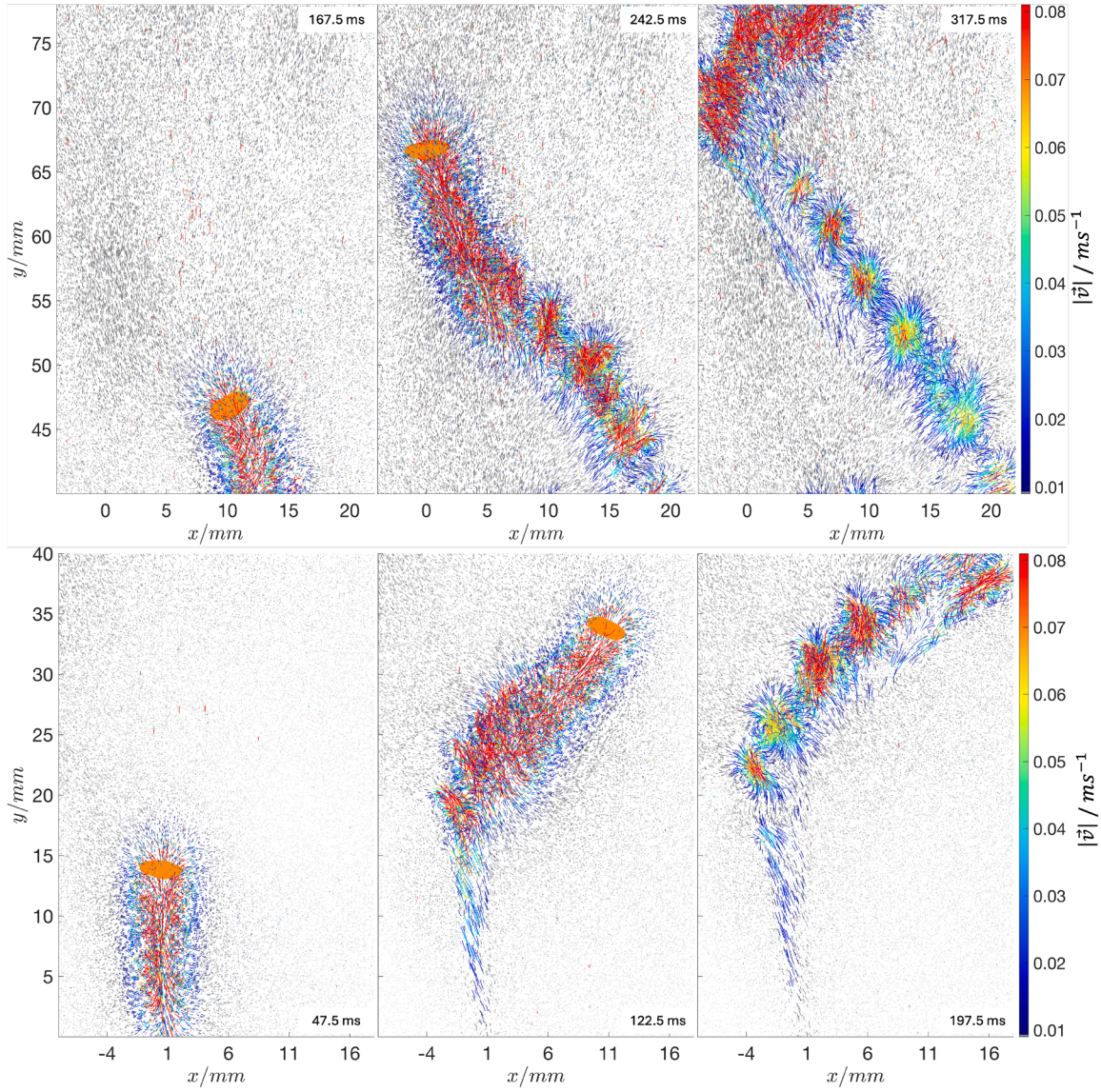

Fig. 6. Tracer particle trajectories with velocity magnitude shown in a color gradient for a bubble equivalent diameter of $d_b = 2.62$ mm. The particle trajectories shown here are those that are retrieved from the DAVIS software without any further postprocessing. The slow, barely moving particles are shown in light gray to improve the visualization. The figure is to be read from the lower left to the upper right. The timestamps indicate the elapsed time after bubble detachment in the corner of each image.

Table 2
Dimensionless numbers and comparison to similar studies.

Authors	d_b/mm	$\lvert\vec{u}_{rise}\rvert$ /m s^{-1}	Eo	Re	$Mo\,[10^{-11}]$	Ga
this work	2.45 ± 0.1	0.321	0.810	822	2.14	397
this work	2.62 ± 0.1	0.295	0.926	808	2.14	439
Lunde and Perkins (1998) (exp.)	2.4	0.326	–	991	–	–
Huang and Saito (2017b,a) (exp.)	2.98	0.303	1.20	1012.1	1.66	–
Cano-Lozano et al. (2016) (num.)	Case 5	–	0.55	–	1.11	350.2
Lee and Park (2022) (exp.)	2.46	0.334	0.82	821	–	–
Lee and Park (2022) (exp.)	2.62	0.350	0.94	912	–	–
Chang et al. (2023) (exp.)	2.4 ± 0.1	0.320	0.80	760	2.56	367

slightly decreasing terminal rise velocity for the larger bubble despite the growing bubble diameter in the observed bubble size regime.

3.2. Particle tracks and velocities

The analysis of the tracer particle trajectories derived from the 4D-PTV measurements provides valuable insight into both the motion of the tracer particles and the general flow field induced by the rising bubble (Fig. 5 and Fig. 6). On average, more than 67,000 particles were detected and analyzed in each image. Notably, approximately one third of these particles are followed throughout the entire measurement duration (≈ 1 s), representing the flow over the full observation period. The remaining particles are only tracked for shorter intervals, as they either left or entered the measurement volume during the recording or were

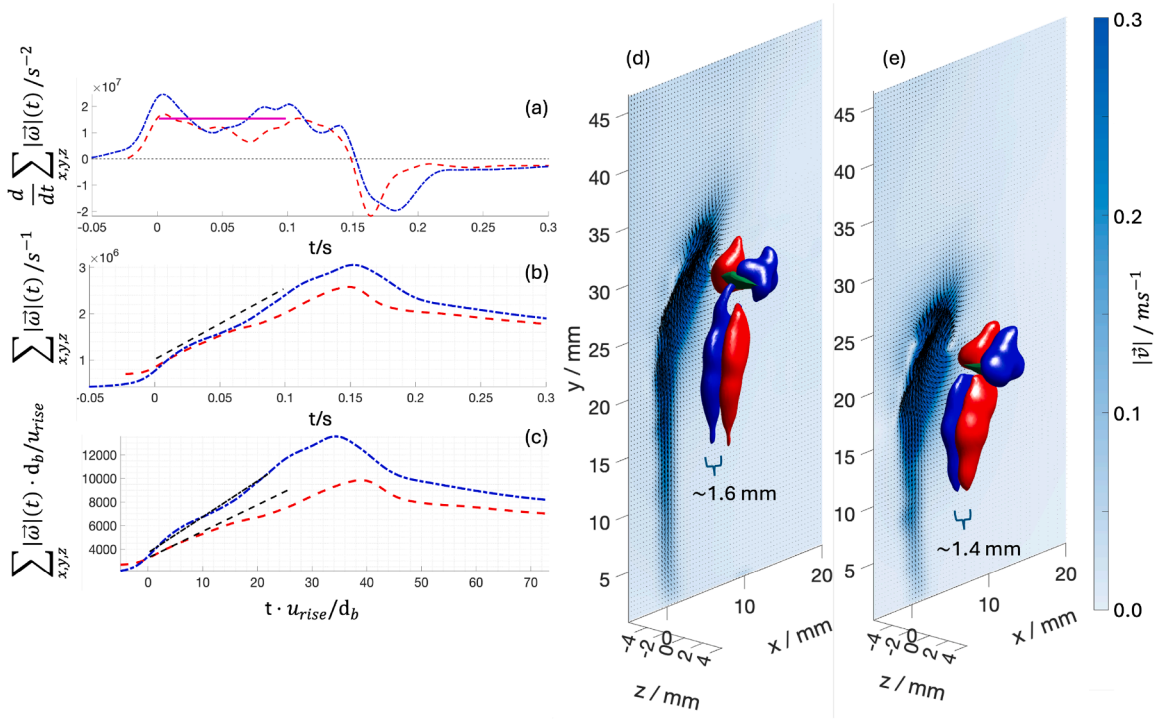

Fig. 7. Temporal evolution of the total vorticity magnitude $\sum_{x,y,z} |\vec{\omega}|(t)$ in the wake of rising bubbles with diameters of 2.45 mm (red dashed line) and 2.62 mm (blue dash-dotted line). **(a)** Time derivative of the vorticity magnitude $\frac{\mathrm{d}}{\mathrm{dt}} \sum_{x,y,z} |\vec{\omega}|(t)$; the pink solid line indicates the estimated linear growth rate during the early development phase. The corresponding linear growth is highlighted by the black dashed line in (b) and the rescaled black dashed lines in (c). **(b)** Time evolution of the total vorticity magnitude $\sum_{x,y,z} |\vec{\omega}|(t)$. **(c)** Vorticity scaled by the bubble diameter d_b and terminal rise velocity u_rise as a function of the non-dimensional time $t \cdot u_\mathrm{rise}/d_\mathrm{b}$. **(d, e)** Three-dimensional visualization of isosurfaces of the y-component of the vorticity (red for $\omega_y = 7\,s^{-1}$ and blue for $\omega_y = -7\,s^{-1}$) in the wake of the rising bubbles with diameters of $d_\mathrm{b} = 2.45$ mm ($t = 0.0725$ s after bubble detachment) (d) and $d_\mathrm{b} = 2.62$ mm ($t = 0.1013$ s after bubble detachment) (e) when the generation of secondary vortices starts. Black arrows indicate every second in-plane velocity vector and the background color map shows the velocity magnitude $|\vec{v}|$ in the central (y, z)-plane. The approximate vortex core spacing is annotated below the vortices.

lost by the STB algorithm for some time steps. Five repetitions of the experiment for each bubble size and recording volume showed so little variations that only one dataset of tracer particles of each experimental setting is shown here.

For both bubble sizes, tracer particles are displaced upwards by the direct influence of the ascending pushing motion of the bubble. As the bubble continues to rise, a recirculating region becomes evident, with particles being drawn back into the bubble's wake. Within this region, numerous small-scale, circular trajectories are observed, indicating the presence of rotational or swirling flow components. A clear acceleration of the particles in the positive y-direction, the direction of bubble ascent, is observable in the immediate wake region behind the bubble. The tracer particles are somewhat slower than the bubble's rise velocity, reaching velocities of up to 0.12 m/s.

When the bubble begins to rotate and drift laterally in the positive x-direction, the particle trajectories undergo significant changes. New flow patterns appear, characterized by particle paths deviating from the primary ascent direction of the bubble at angles approaching 90 degrees. Over time, these trajectories evolve into intricate, spatially extended structures that indicate the development of vortices or, at minimum, strong lateral shear and rotational flow. It is evident that particle velocities within these features remain elevated over extended periods and that the structures are interconnected. As a result, particle trajectories can be seen to form part of multiple of these specific high velocity flow regions.

A comparable behavior is observed for both bubble sizes, with the distinction that the number of velocity-enhanced structures varies depending on the bubble diameter. While these features strongly suggest vortex-like dynamics in the Eulerian velocity field the identification of actual vortices in the velocity field requires the evaluation of vorticity fields. These are computed from Eulerian velocity fields that are reconstructed from the Lagrangian particle trajectories obtained via 4D-PTV.

3.3. Vortical structures in the bubble wake

The rising bubbles feed energy into the flow and produce vorticity in the flow. Vorticity is the local rotation of the fluid parcels and the vorticity field is calculated by $\vec{\omega}(x, y, z, t) = \nabla \times \vec{v}(x, y, z, t)$. The vorticity field is computed from the interpolated velocity fields obtained via the 4D-PTV measurements as described above. As long as the bubble rises through the field of view, it is expected that the overall vorticity increases, since a body moving in a viscous fluid generates vorticity on its surface (Legendre, 2007). Furthermore, in this experiment the bubbles are the only source of vorticity and fluid motion in general. Fig. 7 illustrates the temporal evolution of the total vorticity magnitude $\sum_{x,y,z} |\vec{\omega}|(t)$, calculated by summing vorticity of all voxels, in the wake of the rising air bubbles with diameters of $d_\mathrm{b} = 2.45$ mm (red dashed lines) and $d_\mathrm{b} = 2.62$ mm (blue dash-dotted lines).

Fig. 7(a) shows the time derivative of the total vorticity magnitude, $\frac{\mathrm{d}}{\mathrm{dt}} \sum_{x,y,z} |\vec{\omega}|(t)$, highlighting the rate of vorticity production after bubble detachment. The magnitude of the vorticity of each time step shows fluctuations and is therefore smoothed with a Gaussian using the built-in MATLAB function *smoothdata* with a window width of 30 time steps. During the early phase of the bubble ascent, approximately from $t = 0$ s to $t = 0.1$ s, a positive derivative is observed that can be approximated by a constant α_const complying with a linear increase in vorticity (see magenta line in panel (a) and black lines in panel (b) and (c)). This behavior is consistent with the perpetual formation of vortex structures in

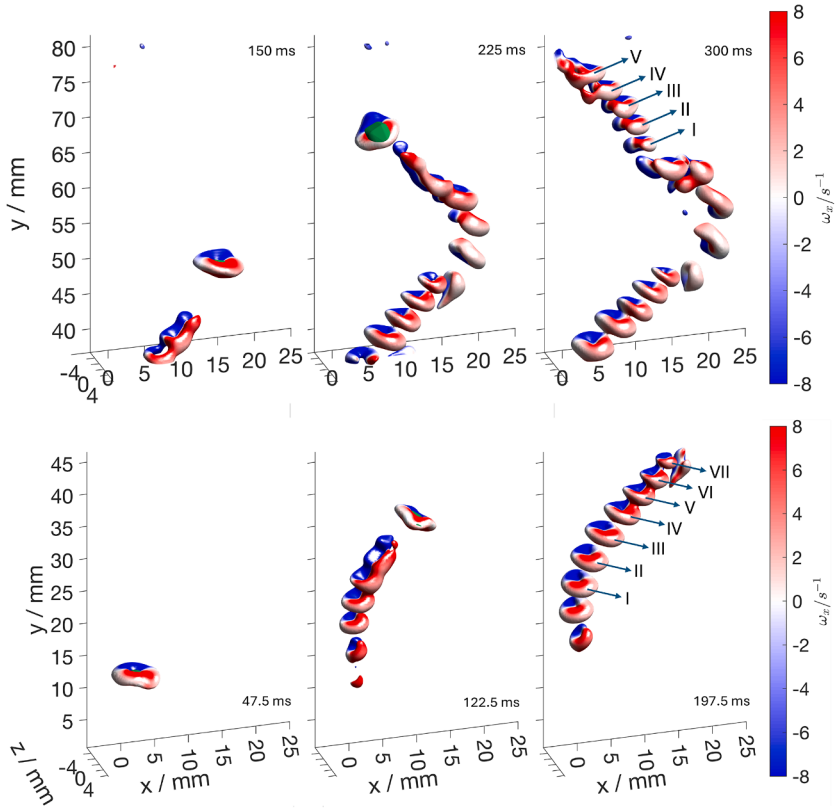

Fig. 8. Development of the vortex structures in the wake of the bubble, visualized using the Q-criterion. The bubble ($d_b = 2.45$ mm) is shown in green but it is not clearly visible in all images due to the vortex surrounding it and because for the rightmost panels the bubble has left the measurement volumes already. The Q-values were calculated from 3D interpolated velocity fields and smoothed with a Gaussian filter. The vortex structures are represented as Q-isosurfaces ($Q = 3\,\mathrm{s}^{-2}$), colored by the interpolated ω_x. The figure is to be read from the lower left to the upper right according to the timestamps after bubble detachment in the corner of each image.

the near wake of the bubble after detachment. To estimate the vorticity that is produced directly on the bubble interface at each moment, this constant vorticity production rate can be integrated in time

$$\sum_{interface} |\vec{\omega}| = \int_0^{t_{\mathrm{flow}}} \alpha_{\mathrm{const}}\,\mathrm{dt} = \alpha_{\mathrm{const}} \cdot t_{\mathrm{flow}} \tag{6}$$

which results in $\sum_{interface} |\vec{\omega}| = 1.85 \times 10^5\,\mathrm{s}^{-1}$ for the smaller bubble and $\sum_{\mathrm{interface}} |\vec{\omega}| = 2.15 \times 10^5\,\mathrm{s}^{-1}$ for the larger bubble, where $t_{\mathrm{flow}} = \pi \cdot d_b/|\vec{u}_{\mathrm{rise}}|$ is the average time it takes for a fluid parcel to pass the bubble ($t_{\mathrm{flow}} = 0.012$ s and $t_{\mathrm{flow}} = 0.014$ s for the smaller and larger bubble respectively). Another approach to extract the generated vorticity at the bubble from the measured data is to consider the interfacial vorticity at the bubble surface in each moment as was recently done for numerical data and spherical bubbles with different surfactant contamination levels (Hayashi et al., 2025). However, this interfacial vorticity cannot be approximated for this dataset yet, as the bubble interface is currently not sufficiently well resolved in the z-direction. Despite this limitation, the obtained value of the overall vorticity generated in every moment can serve as a basis for comparison and validation for numerical simulations and, to the best knowledge of the authors, has not been measured experimentally before considering all three vorticity components. In principle, the average drag force can be deduced from the vorticity by correlations of the maximal vorticity at the bubble surface and the drag force, as was derived by numerical studies for ellipsoidal bubbles with uncontaminated surfaces (Legendre, 2007). The study from Legendre showed that the maximal vorticity of ellipsoidal bubbles at the bubble surfaces is a multiple of that of a spherical bubble (up to ten times higher) and depends on the aspect ratio of the major and minor axis of the ellipsoid and the bubble Reynolds number. The increase in vorticity is attributed to the increase in surface curvature for larger aspect ratios. A comparison of the vorticity produced at the bubbles at each moment, as calculated above, with the theoretical prediction of Legendre shows that it exceeds the theoretical value by a factor of ≈ 2. For the comparison, it is assumed that the maximal vorticity calculated by the correlations given in the reference is found at each point of a sphere with the equivalent diameter of the studied bubbles which surely is an overestimation and further increases the discrepancy to the showcased measurements. However, the high value might also be an effect of a slight surfactant contamination at the bubble surface due to unintended impurities from laboratory conditions (no clean room). The effect that surfactants increase the vorticity production at the bubble has recently been shown numerically for spherical bubbles by Hayashi et al. (2025) and previous work (Pesci et al., 2018; Weiner et al., 2019; Weiner, 2020). To the knowledge of the authors, no experimental measurements have been performed that evaluate the produced vorticity at the bubble surface for rising ellipsoidal bubbles in quiescent water. The performed measurement analysis provide a procedure for comparing the experimentally derived data to numerical results in the future.

Fig. 7(b) presents the total vorticity $\sum_{x,y,z} |\vec{\omega}|(t)$ as a function of time for both bubble sizes, revealing a clear linear increase in the wake vorticity following bubble detachment. The slope from the pink line in Fig. 7(a) is highlighted by the dashed black line in 7(b). The total vorticity reaches a maximum at $t \approx 0.148$ s for the smaller bubble and $t \approx 0.153$ s for the larger bubble, which correspond to the moments when the bubbles exit their respective measurement volume. Following this point, the total vorticity begins to decrease, as also the associated vortex structures are advected out of the observation domain and start to

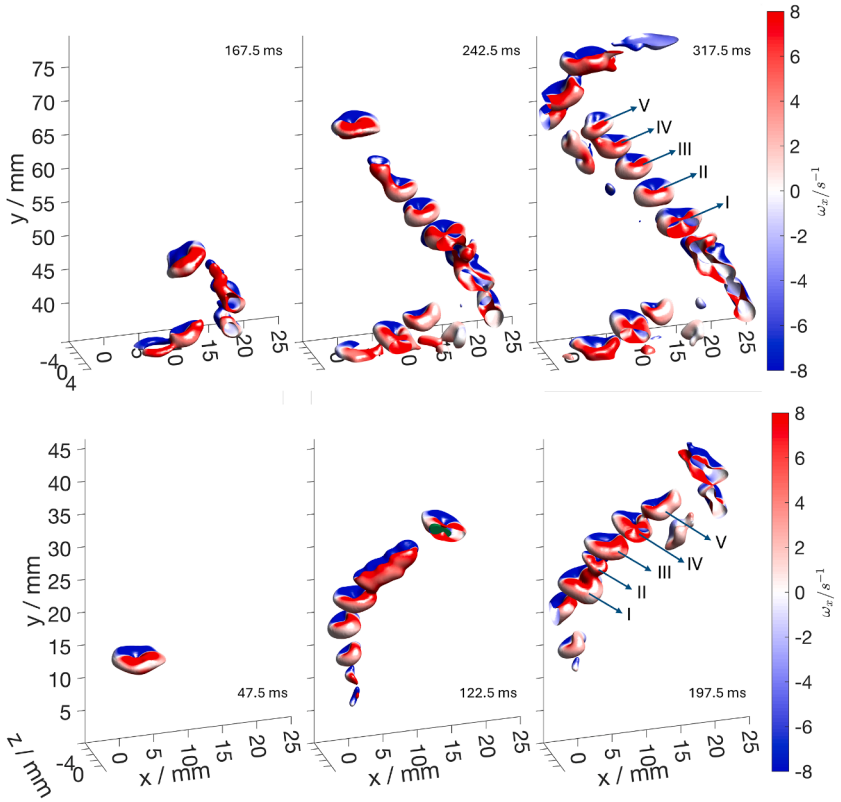

Fig. 9. Development of the vortex structures in the wake of the bubble, visualized using the Q-criterion. The bubble ($d_b = 2.62$ mm) is shown in green. The Q-values were calculated from 3D interpolated velocity fields and smoothed with a Gaussian filter. The vortex structures are represented as Q-isosurfaces ($Q = 3\,s^{-2}$), colored by the interpolated ω_x. The figure is to be read from the lower left to the upper right according to the timestamps after bubble detachment in the corner of each image.

decay. Notably, the larger bubble (2.62 mm) generates more vorticity than the smaller one, in correspondence with the increased wake volume and slower bubble rise.

Fig. 7(c) displays the same total vorticity data as (b) but in a dimensionless representation: time is normalized by the bubble equivalent diameter d_b and terminal rise velocity u_{rise}, and the vorticity is scaled by d_b/u_{rise} (Legendre, 2007), yielding the dimensionless vorticity $\sum_{x,y,z} |\vec{\omega}|(t) \cdot d_b/u_{rise}$. This normalization allows for a comparison with existing literature (Legendre, 2007) and supports a generalizable interpretation of the wake dynamics. Both bubbles also exhibit an initial linear increase in normalized vorticity. However, the increase in normalized vorticity in (c) is considerably steeper for the larger bubble and two different slopes arise due to the non-dimensionalisation, highlighted by two different dashed lines. Interestingly, in the dimensionless representation the larger bubble reaches the maximal vorticity ahead of the smaller bubble.

Fig. 7(d) and (e) provide three-dimensional visualizations of the wake flow fields at times when the generation of secondary vortices start for the $d_b = 2.62$ mm and $d_b = 2.45$ mm bubble, respectively. Red and blue isosurfaces represent the y-component of the vorticity, indicating the presence of counter-rotating vortex structures as reported before for the streamwise vorticity for a zig-zagging bubble in silicone oil (Zenit and Magnaudet, 2009). The black arrows on the background slice depict every second central (y, z)-plane velocity vector, while the color code illustrates the velocity magnitude $|\vec{v}|$ in the same central plane. The indicated vortex core spacing of approximately 1.6 mm and 1.4 mm for the smaller and larger bubble, respectively, somewhat contradicts prior observations which report that the wake morphology scales with bubble size (Cano-Lozano et al., 2016). However, the two bubbles studied here have very similar dimensions and therefore, the vortex core spacing is also similar.

Knowing about the evolution of the total vorticity a more detailed look at the vortex structures that form behind the bubble is desirable. Identification of vortex structures in turbulent flows plays a central role in fluid mechanics and aerodynamics. One of the most commonly used methods is the Q-criterion, which was introduced by Hunt et al. (1988). It is based on a mathematical analysis of the velocity gradients and enables an versatile and numerically efficient detection of vortices. The Q-criterion compares vorticity and strain rate and can be described with the formula (Jeong and Hussain, 1995):

$$Q = \frac{1}{2}\left(\|\Omega\|^2 - \|S\|^2\right) \tag{7}$$

Here, the symmetric strain rate tensor S describes local deformation, while the antisymmetric vorticity tensor Ω represents local rotation. In vortex regions, the vorticity magnitude dominates over the strain rate magnitude, i.e.,

$$||\Omega||^2 > ||S||^2$$

As a result, a positive Q-criterion ($Q > 0$), indicates a vortex. Despite its broad application, it must be acknowledged that the Q-criterion, like the other second generation vortex detection methods, exhibit certain limitations in its applicability, especially when looking at the rather arbitrary threshold values. To overcome those shortcomings third generation vortex identification methods were introduced, expanding the potential for vortex detection in turbulent flows (Liu et al., 2016, 2018; Dong et al., 2019; Liu et al., 2019). However, here the focus is primarily on vortex visualization and therefore, the Q-criterion is used for simplicity as in recent literature (Cano-Lozano et al., 2016; Lee and Park, 2022; Chang et al., 2023). Furthermore, the location and existence of the vortices is independent of the threshold value of Q for the data shown

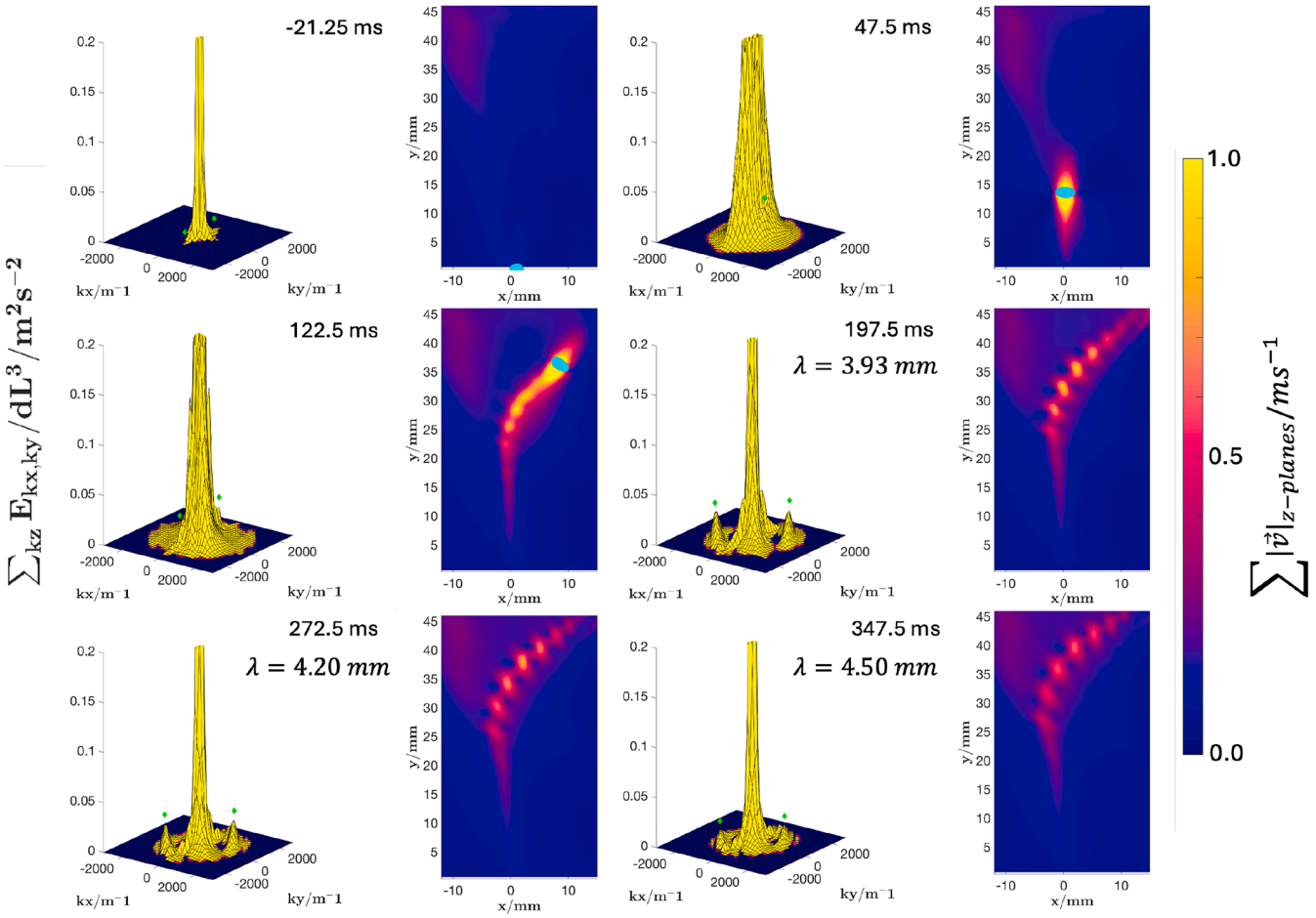

Fig. 10. The energy spectrum in $[k_x, k_y]$ is shown on the left panels for different time steps of the same bubble rise of the smaller bubble ($d_b = 2.45$ mm) during its rise from the needle tip (from upper left to lower right, timesteps in corner of each subplot with regard to bubble detachment). The energy in k-space is divided by $dL^3 = dx \cdot dy \cdot dz$ to keep the units of $m^2 s^{-2}$ of a squared velocity. The energy spectrum is calculated in 3D-space from the velocity for each time-step and then a summation over the third dimension z (depth) is performed for better clarity of the visualization. On the right tiles the corresponding velocity magnitude fields of the same time step are shown, also summed over z, $\sum_z |\vec{v}|$/mm s^{-1} as a color code. The bubble is drawn in turquoise color.

as long as it is positive and larger than zero, while the size of them grows steadily when the threshold is lowered. The vortex cores remain also unchanged when using the λ_2-criterion, another second generation vortex identification method introduced by Jeong and Hussain (1995). Also, since the bubble rises in quiescent liquid, there was no strong shear flow which is known to bias the second generation vortex identification methods. For subsequent studies, however, the third generation vortex identification methods can further clarify the details of the vortex formation, evolution and merging, broadening the scope of the application.

Figs. 8 and 9 represent regions where the Q-criterion exceeds a threshold of $Q = 3\,s^{-2}$, revealing vortex cores for the smaller and the larger bubble, respectively. In the lower panels, the wake structures up to the second inversion section can be observed while in the upper panels, the structures from the second inversion section onwards up to a third inversion section can be seen. For the five equal recordings of equally produced bubbles of the same size it was observed that not only the bubble trajectory is almost identical, but also the formation of the vortex structures shows very similar behavior. During the bubble rise, a vortex and high vorticity is always measured in the direct vicinity of the bubble. Vortices in the wake of the bubble reach their evolved form only after the bubble has risen further. These vortices can be described as torus- or ring- shaped. Vortex structures in the wake of rising bubbles were also identified in the experiments conducted by Chang et al. (2023) and Lee and Park (2022). The measurement by Chang et al. were performed at a height of 200 mm above the needle tip and involved slightly smaller bubbles with a diameter of 2.4 mm where a total of five individual vortices determined by the Q-criterion were observed, albeit less clearly. The measurements of Lee and Park (2022) also used this slightly smaller bubble size and measured the two dimensional velocity field right after bubble detachment. However, likely due to their single plane measurements only the cut through four vortex rings can be detected in between the first and the second inflection section. In their measurements at 200 mm above the needle tip there are only 3 vortex rings distinguishable. However, this can be an effect of the out of plane movement of the bubble. In comparison, the high-resolution and three dimensional measurements reported in this article allow for a more detailed characterization of the vortex rings, particularly in the early stages of bubble rise. In the first inversion section seven vortices ($d_b = 2.45$ mm) and five vortices ($d_b = 2.62$ mm) are identified, respectively, all marked in roman numbers in Figs. 8 and 9 in the rightmost panels. In the second inversion section, both bubble sizes cause five vortex structures which corresponds to the count of Chang's study (Chang et al., 2023).

When examining the vortices generated in the wake of the smaller bubble in Fig. 8 the regularity in form and distance of the vortices is immediately apparent. The vortices of similar size rise in a chain one behind the other and do not interact with each other. Thereby, the vortices move slowly apart from each other and towards negative x-values to the left upper corner. This behavior causes them to be very persistent in time. In contrast, the vortices produced by the larger bubble

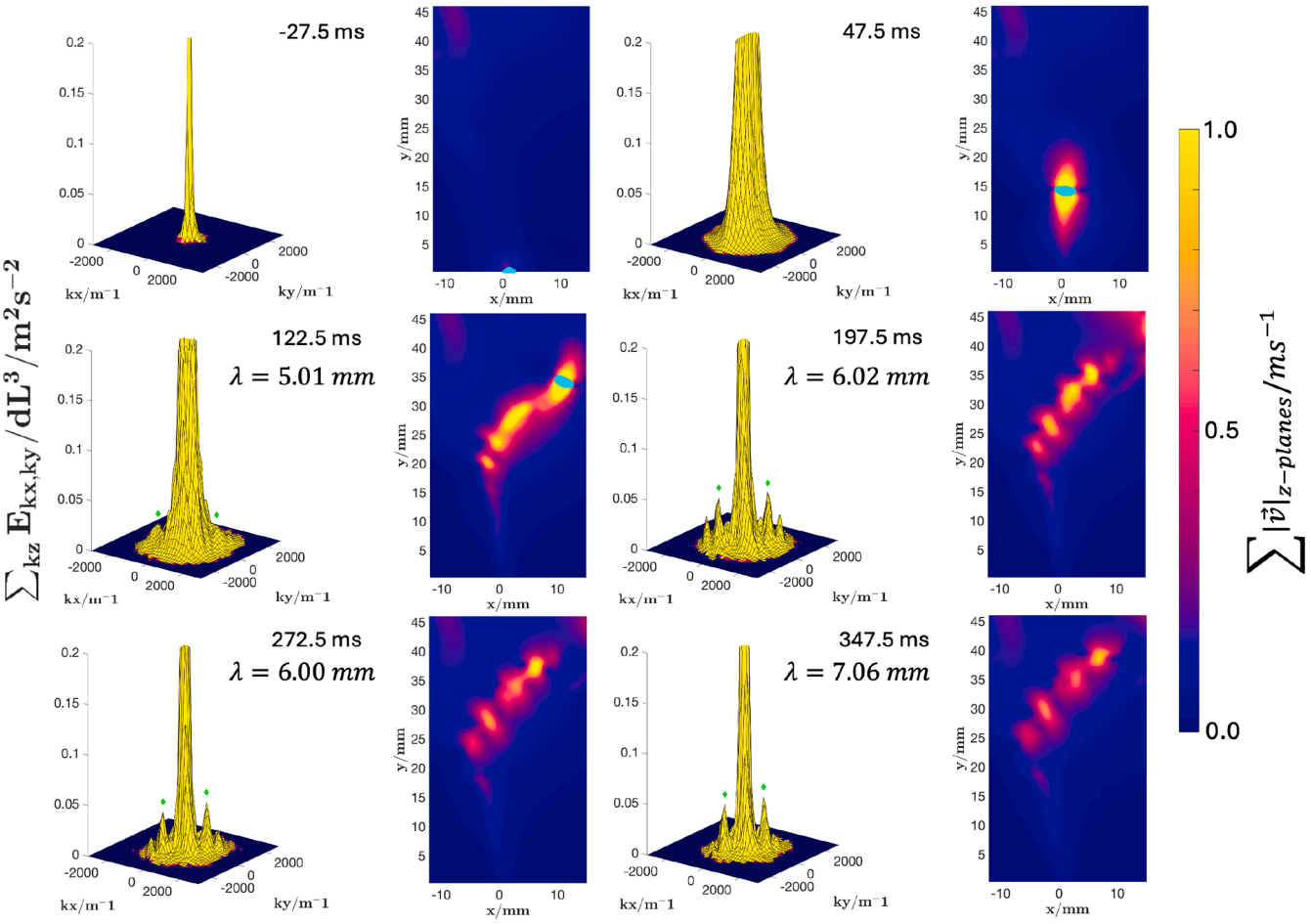

Fig. 11. The energy spectrum in $[k_x, k_y]$ is shown on the left panels for different time steps of the same bubble rise of the larger bubble ($d_b = 2.62$ mm) during its rise from the needle tip (from upper left to lower right, timesteps in corner of each subplot with regard to bubble detachment). The energy in k-space is divided by $dL^3 = dx \cdot dy \cdot dz$ to keep the units of m^2s^{-2} of a squared velocity. The energy spectrum is calculated in 3D-space from the velocity for each time-step and then a summation over the third dimension z (depth) is performed for better clarity of the visualization. On the right tiles the corresponding velocity magnitude fields of the same time step are shown, also summed over z, $\sum_z |\vec{v}|$/mm s^{-1} as a color code. The bubble is drawn in turquoise color.

of $d_b = 2.62$ mm behave differently: The vortex structures are notably larger and exhibit irregularities and more vortex-vortex interaction. As a result, the vortices are more challenging to distinguish and separate, and show some merging over time and are thus less persistent in time. More precisely, vortices 2 and 3 merge, after interacting with each other, at time $t = 0.2988$ s after bubble detachment. Nevertheless, it can generally be stated that the absolute value of the vorticity in the wake of larger bubbles is significantly higher and the size of the vortices and the mean distance in between the vortices are larger.

Cano-Lozano et al. (2016) studied the details of the vortices arising in the bubble wakes using the λ_2-criterion, introduced by Jeong and Hussain (1995), for very similar dimensionless numbers numerically. Especially their case 5 bubble with a similar Galilei number of $Ga = 350$ and a slightly lower Eötvös number of $Eo = 0.55$ shows very similar wake vorticity configurations as reported here for the smaller bubble. They call the observed vortices "secondary vortex loops" with a wavelength in between the different loops Λ that is slightly higher than the spacing between the two vortex threads. Cano-Lozano et al. (2016) attribute the secondary vortex loops to a coupling between the bubble deformation and the wake dynamics which causes a transient asymmetry in the vortex threads. Their hypothesis is supported by the ratio of the typical secondary vortex loops structure wavelength to the equivalent bubble diameter to be $\Lambda/d_b \approx 1.21$. To determine this value for the two bubble sizes investigated here, the vertical distances between two consecutive vortices are measured. Since Cano-Lozano et al. did not specify how they determine the vortex structure wavelength or at what time after vortex formation the distances were taken, thus the average vertical distance (only in y-direction) between two vortices from the first inversion section is used here. This yields a vortex loop distance of $\Lambda = 2.74$ mm for the smaller bubble with $d_b = 2.45$ mm and $\Lambda = 2.75$ mm for the larger bubble with $d_b = 2.62$ mm, which are nearly identical and similar to the vortex distances in y-direction for the single rising bubble in Lee and Park (2022) which seems to be $\Lambda \approx 2.5$ mm when determined from their figures. However, the vortex distances of the larger bubble wake vary more, which is not captured by the mean value. The corresponding ratios Λ/d_b are $\Lambda/d_b = 1.12$ for the smaller bubble and $\Lambda/d_b = 1.05$ for the larger bubble. The value obtained for the smaller bubble is very close to that reported by Cano-Lozano et al. (2016). Moreover, the vortex structures observed in the present measurements and in Cano-Lozano exhibit nearly identical patterns, which do not interact with each other in the bubble wake. In contrast, for the larger bubble, the merging of two vortices is already observed. The experimentally obtained data are in strong agreement with the numerical results of Cano-Lozano et al. (2016) and demonstrate that the phenomena of secondary vortex loops can be found consistently in both numerical simulations and experimental observations.

3.4. Spectral analysis of the wake structures

The spectral analysis of the velocity field gives some insight into the temporal and spectral evolution of the kinetic energy. Figs. 10 and 11 show the energy spectrum in 3D-space calculated from the velocity

field for the lower measurement volume (up to the second inflection section) for the smaller and the larger bubble size, respectively. Three of the time steps shown are those also chosen for Figs. 5, 6, 8 and 9. One more timestep, before the bubbles detach (negative time) and two more time-steps after the bubbles have left the field of view are further considered. The energy spectrum and the corresponding velocity magnitude field are summed up over the third dimension z (depth) for better clarity of the visualization and inspection of the main velocity structures.

To begin with, the high velocity regions in the bubble wake, observed in the particle tracks can also be appreciated in the velocity magnitude fields. These areas of high velocity become increasingly pronounced after the bubble has left the field of view. They correspond to the vortex cores of the previously analyzed vortices. For the smaller bubble of $d_b = 2.45$ mm equivalent diameter, these areas of high velocities are, as the vortices in Fig. 8, very ordered. The imprint of these structures in the energy spectrum are the highest peaks indicated by green dots (two peaks because of the Fourier-space symmetry) in Fig. 10, middle pane, right. The corresponding peak wavelength of these structures that gather the energy, is calculated from the values of k_x and k_y of the peak to be $\lambda_p = 3.93$ mm. This wavelength determined from the energy spectrum corresponds roughly to the distance s_v in between the centers of the vortex rings in Fig. 8 at time $t = 197.5$ ms after detachment, which has been determined to be $s_v = 3.64$ mm. The slight deviation in between λ_p and s_v might be caused by the summation of the energy spectrum in z, while the vortex cores in Fig. 8 are considered in a single plane. At successive times, the vortices drift further apart from each other, towards the upper left corner of the image towards negative x-values. This is also observed in the areas of high velocity and it is reflected in the increasing wavelength of the peaks and the corresponding high velocity structures in time. At $t = 347.5$ ms after bubble detachment the wavelength of the peak is $\lambda_p = 4.50$ mm. Also in Fig. 10, the persistence of the vortex structures for the small bubble can be appreciated, since the structures barely change in shape over time and no vortex interaction or merging can be distinguished, even after the bubble left the measurement volume.

For the larger bubble of $d_b = 2.62$ mm equivalent diameter, the occurring velocity structures are considerably more disordered. The vortices II and III cannot be distinguished from each other in Fig. 11 and vortex IV is only distinguishable at timestep $t = 197.5$ ms, where the bubble has just left the field of view. Also, more peaks appear than for the smaller bubble, indicating that the energy is distributed across more structures with different wavelengths. This corresponds to the fuzzy appearance of the high magnitude velocities. As for the smaller bubble due to increased separation but additionally due to merging, the distances between the structures become larger for longer times after bubble detachment. At timestep $t = 197.5$ ms the first peaks appear. Here, the wavelength of the velocity field structure with the most energy is $\lambda_p = 6.02$ mm. This is considerably higher than the value of the mean distance in between the centers of the vortex rings in Fig. 9 at the same timestep, which has been determined to be $s_v = 4.35$ mm. However, this is most likely an effect of the summation of the energy spectrum in z-direction which impedes a distinction of vortex ring II and III in the energy spectrum. As for the smaller bubble, the vortex rings start to drift apart towards lower x-values and higher y-values. This causes the peak wavelength to progressively increase with time from $\lambda_p = 5.01$ mm at time $t = 122.5$ ms after detachment to $\lambda_p = 7.06$ mm at time $t = 347.5$ ms. The magnitude of the velocities also rapidly decreases. The analysis of the energy spectrum of the wake of the rising bubbles allows to quantify the energy distribution across the velocity field structures. These energy spectra could be used as an experimental basis to generate a spectral forcing source term in Fourier-space (Eswaran and Pope, 1988) to add the effect of bubble wakes to a flow without having to calculate the individual bubbles. This would provide a way to efficiently simulate bubble induced turbulence numerically.

4. Conclusion

This work presents temporarily resolved 3D Particle-Tracking Velocimetry measurements of single rising bubbles with equivalent diameters of $d_b = 2.45$ mm and $d_b = 2.62$ mm in quiescent bidistilled water. The flow is seeded with tracer particles of diameter $d_{tracer} = 19$ µm yielding a very small Stokes number of $St \approx 3 \cdot 10^{-4}$, ensuring flow following behavior. Particle motion is evaluated from bubble detachment to a rising height of 80 mm using the Shake-the-Box algorithm implemented in DaVis. In addition, the 3D bubble shape and rise dynamics are measured to relate bubble motion to the induced flow. On the basis of the performed experiments and the subsequent velocity field analysis the following results can be summarized:

(1) The performed measurements enable a precise determination of velocity fields and its gradients and thus the analysis of the evolving vorticity and energy formation in the bubble wake flow. The obtained data can aid validation of numeric approaches.
(2) The secondary vortex loops predicted by numerical investigations from Cano-Lozano et al. (2016) have been confirmed experimentally. The vortex loops are more persistent and ordered for the smaller bubble which suggests that they occur only within a narrow parameter range and that slightly larger bubbles already alter the system dynamics. Here, a detailed numerical study could be of further interest.
(3) This work is the first experimental analysis of the total vorticity production by ellipsoidal bubbles, exceeding the predictions for clean bubbles stated by Legendre (2007).
(4) The analysis of the energy spectra during the bubble rise provides a basis for numerical studies to design a realistic forcing term, that reflects the way that bubbles induce energy into the bulk flow.

In future work, the determined resulting particle tracks and the derived velocity fields can be used to study mass transfer in the bubble wake. Also, the flow data can be compared to existing studies on the mass transfer of bubbles with comparable dimensionless parameters. Moreover, the concept of coherent Lagrangian structures occurring in bubble wakes, as in Kameke et al. (2019a), can be extended to freely rising bubbles. Further emphasis can now be placed on improved reconstruction of the bubble shape and flow measurements in bubble swarms where third generation vortex detection methods, as stated by Liu et al. (2019), should be considered for more precise evaluation of interacting vortex structures.

CRediT authorship contribution statement

A.v. Kameke: Writing – review & editing, Writing – original draft, Visualization, Validation, Supervision, Software, Resources, Project administration, Methodology, Investigation, Funding acquisition, Formal analysis, Data curation, Conceptualization; **R. Uphoff:** Writing – original draft, Visualization, Methodology, Investigation, Data curation; **E. Steuwe:** Writing – review & editing, Software, Formal analysis, Data curation; **J. H. Nissen:** Writing – review & editing, Methodology, Investigation; **M. Hoffmann:** Writing – review & editing, Resources, Project administration, Conceptualization; **M. Schlüter:** Writing – review & editing, Supervision, Resources, Project administration, Conceptualization; **F. Kexel:** Writing – review & editing, Writing – original draft, Project administration, Methodology, Investigation, Formal analysis, Data curation.

Data availability

The particle trajectory data as obtained after analysis with Shake-the-Box using DaVis 11.0 software (LaVision GmbH, Germany) and the bubble outline data generated with MATLAB (r2024a), as well as some scripts to process the data can be found here: https://doi.org/10.15480/882.16589. Raw camera recording data can be made available upon request to the corresponding author.

Declaration of competing interest

The authors declare that they have no known competing financial interests or personal relationships that could have appeared to influence the work reported in this paper.

Acknowledgements

This work is funded by the Deutsche Forschungsgemeinschaft (DFG, German Research Foundation) - 517064495 and CRC 1615 “SMART Reactors” 503850735. The major instrumentation device MUST, funded by the Deutsche Forschungsgemeinschaft (DFG, German Research Foundation) - 514139948, has been used for the measurements. The authors thank Prof. Dr. Padberg-Gehle (LEUPHANA Lüneburg) and Dr. Tian Ma (Helmholtz-Zentrum Dresden-Rossendorf - HZDR) for fruitful discussions.

References

Adrian, R.J., 1991. Particle-imaging techniques for experimental fluid mechanics. Annu. Rev. Fluid Mech. 23 (1), 261–304. https://doi.org/10.1146/annurev.fl.23.010191.001401

Bhattacharya, S., Vlachos, P.P., 2020. Volumetric particle tracking velocimetry (PTV) uncertainty quantification. Exp Fluids 61 (9), 197. https://doi.org/10.1007/s00348-020-03021-6

Bork, O., Schlueter, M., Raebiger, N., 2005. The impact of local phenomena on mass transfer in gas-liquid systems. Can. J. Chem. Eng. 83 (4), 658–666. https://doi.org/10.1002/cjce.5450830406

Cano-Lozano, J.C., Martínez-Bazán, C., Magnaudet, J., Tchoufag, J., et al., 2016. Paths and wakes of deformable nearly spheroidal rising bubbles close to the transition to path instability. Phys. Rev. Fluids 1 (5), 053604. https://doi.org/10.1103/PhysRevFluids.1.053604

Chang, Y., Müller, C., Kováts, P., Guo, L., Zähringer, K., et al., 2023. Hydrodynamics and shape reconstruction of single rising air bubbles in water using high-speed tomographic particle tracking velocimetry and 3d geometric reconstruction. Exp Fluids 65 (1), 6. https://doi.org/10.1007/s00348-023-03746-0

Clift, R., Grace, J.R., Weber, M.E., 1978. Bubbles, Drops and Particles. Dover Publications, ISBN 978-0-486-4450-9.

Dong, X., Gao, Y., Liu, C., 2019. New normalized Rortex/vortex identification method. Phys. Fluids 31 (1), 011701. https://pubs.aip.org/pof/article/31/1/011701/103475/New-normalized-Rortex-vortex-identification-method. https://doi.org/10.1063/1.5066016

Eswaran, V., Pope, S.B., 1988. An examination of forcing in direct numerical simulations of turbulence. Comput. Fluids 16 (3), 257–278. https://doi.org/10.1016/0045-7930(88)90013-8

Gesemann, S., 2015. From particle tracks to velocity and acceleration fields using b-splines and penalties. Version Number: 1. https://doi.org/10.48550/ARXIV.1510.09034

Hayashi, K., Motoki, Y., Legendre, D., Tomiyama, A., et al., 2025. Drag and interfacial vorticity of spherical bubble contaminated with soluble surfactant. Int. J. Multiphase Flow 187, 105173. https://doi.org/10.1016/j.ijmultiphaseflow.2025.105173

Hoque, M.M., Moreno-Atanasio, R., Doroodchi, E., Joshi, J.B., Evans, G.M., Mitra, S., 2022. Dynamics of a single bubble rising in a quiescent medium. Exp. Therm Fluid Sci. 132, 110546. https://doi.org/10.1016/j.expthermflusci.2021.110546

Huang, G., Liu, B., Song, Y., Yin, J., Wang, D., et al., 2025. 3D measurement of interfacial mass transfer of isolated millimetric bubbles in turbulence: multi-view SI-VILF technique and simultaneous reconstruction of deforming bubble interface and surrounding concentration field. Int. J. Multiphase Flow 184, 105106.

Huang, G., Lv, X., Chen, W., Song, Y., Yin, J., Wang, D., et al., 2024. Measurement of interfacial mass transfer of single bubbles rising in homogeneous turbulence. Chem. Eng. Sci. 288, 119757. https://doi.org/10.1016/j.ces.2024.119757

Huang, J., Saito, T., 2017a. Discussion about the differences in mass transfer, bubble motion and surrounding liquid motion between a contaminated system and a clean system based on consideration of three-dimensional wake structure obtained from LIF visualization 170, 105–115. https://doi.org/10.1016/j.ces.2017.03.030

Huang, J., Saito, T., 2017b. Influences of gas-liquid interface contamination on bubble motions, bubble wakes, and instantaneous mass transfer. Chem. Eng. Sci. 157, 182–199. https://doi.org/10.1016/j.ces.2016.05.013

Hunt, J.C.R., Wray, A.A., Moin, P., 1988. Eddies, streams, and convergence zones in turbulent flows https://www.researchgate.net/publication/234550074_Eddies_streams_and_convergence_zones_in_turbulent_flows

Janke, T., Michaelis, D., 2021. Uncertainty quantification for PTV/LPT data and adaptive track filtering. ISPIV21 1 (1). https://doi.org/10.18409/ispiv.v1i1.125

Jeong, J., Hussain, F., 1995. On the identification of a vortex. J. Fluid Mech. 285, 69–94. https://www.cambridge.org/core/product/identifier/S0022112095000462/type/journal_article. https://doi.org/10.1017/S0022112095000462

Jin, Y., Cavero, R.F., Weiland, C., Hoffmann, M., Schlüter, M., et al., 2023. Effects of bubble-induced turbulence on interfacial species transport: a direct numerical simulation study. Chem. Eng. Sci. 279, 118934.

Jin, Y., Schlüter, M., 2019. Direct numerical simulation of the interfacial mass transfer of a bubble in self-induced turbulent flows. Int. J. Heat Mass Transf. 135, 1248–1259. https://doi.org/10.1016/j.ijheatmasstransfer.2019.02.067

Kameke, A.v., Kastens, S., Rüttinger, S., Herres-Pawlis, S., Schlüter, M., 2019a. How coherent structures dominate the residence time in a bubble wake: an experimental example 207, 317–326. https://doi.org/10.1016/j.ces.2019.06.033

Kameke, A.v., Kexel, F., Rüttinger, S., Colombi, R., Kastens, S., Schlüter, M., et al., 2019b. 3D-reconstruction of O2 bubble wake concentration fields. Proceedings of 13th International Symposium on Particle Image Velocimetry .

Kexel, F., Kastens, S., Timmermann, J., Kameke, A.v., Schlüter, M., 2021. Reactive bubbly flows-influence of boundary layer dynamics on mass transfer and chemical reactions. In: Reactive Bubbly Flows. Springer Nature. Vol. Fluid Mechanics and Its Applications, vol 128.

Kong, G., Mirsandi, H., Buist, K.A., Peters, E.A.J.F., Baltussen, M.W., Kuipers, J.A.M., et al., 2019. Oscillation dynamics of a bubble rising in viscous liquid. Exp. Fluids 60 (8), 130. https://doi.org/10.1007/s00348-019-2779-1

Lamb, H., 2009. Hydrodynamics. Cambridge mathematical library, Univ. Pr, Cambridge. 6. ed., transferred to digital printing 2006, [nachdr.] edition.

LaVision GmbH, L., 2023. Product Manual for DaVis 11.0. LaVision GmbH, Anna-Vandenhoeck-Ring 19, D-37081 Göttingen Produced by LaVision GmbH, Göttingen.

Lee, J., Park, H., 2022. Flow induced by the single-bubble chain depending on the bubble release frequency. Physics of Fluids 34 (3), 033312. https://doi.org/10.1063/5.0083281

Legendre, D., 2007. On the relation between the drag and the vorticity produced on a clean bubble 19 (1), 018102. https://doi.org/10.1063/1.2430645

Liu, C., Gao, Y., Tian, S., Dong, X., et al., 2018. Rortex-a new vortex vector definition and vorticity tensor and vector decompositions. Phys. Fluids 30 (3), 035103. https://pubs.aip.org/pof/article/30/3/035103/105678/Rortex-A-new-vortex-vector-definition-and. https://doi.org/10.1063/1.5023001

Liu, C., Gao, Y.-s., Dong, X.-r., Wang, Y.-q., Liu, J.-m., Zhang, Y.-n., Cai, X.-s., Gui, N., 2019. Third generation of vortex identification methods: omega and liutex/rortex based systems. J. Hydrodyn. 31 (2), 205–223. https://doi.org/10.1007/s42241-019-0022-4

Liu, C., Wang, Y., Yang, Y., Duan, Z., 2016. New omega vortex identification method. Sci. China Phys. Mech. Astronomy 59 (8), 684711. https://doi.org/10.1007/s11433-016-0022-6

Lunde, K., Perkins, R.J., 1998. Shape oscillations of rising bubbles: this paper is dedicated to professor lee van wijngaarden, whose work and approach to fluid mechanics is an inspiration. In: Biesheuvel, A., Van Heijst, G.F. (Eds.), In Fascination of Fluid Dynamics. Springer Netherlands. Vol. 45, pp. 387–408. Series Title: Fluid Mechanics and its Applications. https://doi.org/10.1007/978-94-011-4986-0_20

Ma, T., Hessenkemper, H., Lucas, D., Bragg, A.D., et al., 2022. An experimental study on the multiscale properties of turbulence in bubble-laden flows. J. Fluid Mech. 936, A42. https://doi.org/10.1017/jfm.2022.86

Magnaudet, J., Eames, I., 2000. The motion of high-reynolds-number bubbles in inhomogeneous flows. Annu. Rev. Fluid Mech. 32 (1), 659–708. https://doi.org/10.1146/annurev.fluid.32.1.659

Matlab (r2024a), 2024. https://www.mathworks.com/products/matlab.html.

Meiron, D.I., 1989. On the stability of gas bubbles rising in an inviscid fluid. J. Fluid Mech. 198, 101–114. https://doi.org/10.1017/S0022112089000054

Motarjemi, M., Jameson, G.J., 1978. Mass transfer from very small bubbles-the optimum bubble size for aeration. Chem. Eng. Sci. 33 (11), 1415–1423. https://doi.org/10.1016/0009-2509(78)85190-2

Ouellette, N.T., O'Malley, P.J.J., Gollub, J.P., 2008. Transport of finite-sized particles in chaotic flow 101 (17), 174504. https://doi.org/10.1103/PhysRevLett.101.174504

Pesci, C., Weiner, A., Marschall, H., Bothe, D., 2018. Computational analysis of single rising bubbles influenced by soluble surfactant. J. Fluid Mech. 856, 709–763. https://doi.org/10.1017/jfm.2018.723

Salibindla, A. K.R., Masuk, A. U.M., Ni, R., et al., 2021. Experimental investigation of the acceleration statistics and added-mass force of deformable bubbles in intense turbulence. J. Fluid Mech. 912, A50. https://doi.org/10.1017/jfm.2020.1121

Salibindla, A. K.R., Masuk, A. U.M., Tan, S., Ni, R., et al., 2020. Lift and drag coefficients of deformable bubbles in intense turbulence determined from bubble rise velocity. J. Fluid Mech. 894, A20. https://www.cambridge.org/core/product/identifier/S002211202000244X/type/journal_article. https://doi.org/10.1017/jfm.2020.244

Schanz, D., Gesemann, S., Schröder, A., et al., 2016. Shake-the-box: Lagrangian particle tracking at high particle image densities. Exp. Fluids 57 (5), 70. https://doi.org/10.1007/s00348-016-2157-1

Schanz, D., Novara, M., Schröder, A., et al., 2021. Shake-the-box particle tracking with variable time-steps in flows with high velocity range (VT-STB). ISPIV21 1 (1). https://doi.org/10.18409/ispiv.v1i1.65

Schanz, D., Schröder, A., Gesemann, S., Michaelis, D., Wieneke, B., 2013. 'shake the box': a highly efficient and accurate tomographic particle tracking velocimetry (TOMO-PTV) method using prediction of particle positions. Pages: 13.

Schlüter, M., Bothe, D., Herres-Pawlis, S., Nieken, U. (Eds.), 2021. Reactive Bubbly Flows. Fluid Mechanics and Its Applications, Springer International Publishing. https://doi.org/10.1007/978-3-030-72361-3

Schröder, A., Schanz, D., 2023. 3D lagrangian particle tracking in fluid mechanics. Annu. Rev. Fluid Mech. 55 (1), 511–540. https://doi.org/10.1146/annurev-fluid-031822-041721

Sciacchitano, A., Wieneke, B., Scarano, F., 2013. PIV uncertainty quantification by image matching. Meas. Sci. Technol. 24 (4), 045302. https://doi.org/10.1088/0957-0233/24/4/045302

Tan, S., Salibindla, A., Masuk, A. U.M., Ni, R., et al., 2020. Introducing OpenLPT: new method of removing ghost particles and high-concentration particle shadow tracking. Exp. Fluids 61 (2), 47. https://doi.org/10.1007/s00348-019-2875-2

Tan, S., Salibindla, A. K.R., Masuk, A. U.M., Ni, R., et al., 2019. An open-source shake-the-box method and its performance evaluation. https://athene-forschung.unibw.de/doc/128860/128860.pdf.

Tomiyama, A., Celata, G.P., Hosokawa, S., Yoshida, S., 2002. Terminal velocity of single bubbles in surface tension force dominant regime. Int. J. Multiphase Flow 28 (9), 1497–1519. https://doi.org/10.1016/S0301-9322(02)00032-0

Weiner, A., 2020. Modeling and simulation of convection-dominated species transfer at rising bubbles. PhD thesis, TU Darmstadt . https://doi.org/10.25534/tuprints-00011405

Weiner, A., Timmermann, J., Pesci, C., Grewe, J., Hoffmann, M., Schlüter, M., Bothe, D., et al., 2019. Experimental and numerical investigation of reactive species transport around a small rising bubble 1, 100007. https://doi.org/10.1016/j.cesx.2019.100007

Wieneke, B., 2008. Volume self-calibration for 3d particle image velocimetry. Exp. Fluids 45 (4), 549–556. https://doi.org/10.1007/s00348-008-0521-5

Wieneke, B., 2018. Improvements for volume self-calibration. Meas. Sci. Technol. 29 (8), 084002. https://doi.org/10.1088/1361-6501/aacd45

Xu, X., Tan, S., Qi, Y., Ni, R., et al., 2025. Experimental investigation of turbulence modulation by deformable bubbles. Phys. Rev. Fluids 10 (3), 033605. https://doi.org/10.1103/PhysRevFluids.10.033605

Zenit, R., Magnaudet, J., 2009. Measurements of the streamwise vorticity in the wake of an oscillating bubble. Int. J. Multiphase Flow 35 (2), 195–203. https://doi.org/10.1016/j.ijmultiphaseflow.2008.10.007